Imaging tunable quantum Hall broken-symmetry orders in charge-neutral graphene

Alexis Coissard, David Wander, Hadrien Vignaud, Adolfo G. Grushin, Cécile Repellin, Kenji Watanabe, Takashi Taniguchi, Frédéric Gay, Clemens Winkelmann, Hervé Courtois, et al.

Imaging tunable quantum Hall broken-symmetry orders in charge-neutral graphene

Alexis Coissard,[1] David Wander,[1] Hadrien Vignaud,[1] Adolfo G. Grushin,[1]
Cécile Repellin,[2] Kenji Watanabe,[3] Takashi Taniguchi,[4] Frédéric Gay,[1] Clemens
Winkelmann,[1] Hervé Courtois,[1] Hermann Sellier,[1] and Benjamin Sacépé[1,*]

[1] *Univ. Grenoble Alpes, CNRS, Grenoble INP, Institut Néel, 38000 Grenoble, France*
[2] *Univ. Grenoble-Alpes, CNRS, LPMMC, 38000 Grenoble, France*
[3] *Research Center for Functional Materials, National Institute for Materials Science, 1-1 Namiki, Tsukuba 305-0044, Japan*
[4] *International Center for Materials Nanoarchitectonics, National Institute for Materials Science, 1-1 Namiki, Tsukuba 305-0044, Japan*

Charge-neutral graphene under perpendicular magnetic field was predicted to harbor a rich variety of many-body ground states with distinct topological and symmetry breaking orders. We directly image the atomic-scale electronic wavefunction of three distinct broken-symmetry phases in graphene using scanning tunneling spectroscopy. We explore the phase diagram by controllably tuning the magnetic field and the screening of the Coulomb interaction by close proximity to a low or high dielectric constant substrate. In the unscreened case, we unveil a Kekulé bond order. Under dielectric screening, a sublattice-unpolarized ground state emerges at low magnetic fields, and transits to a charge-density-wave order with partial sublattice polarization at higher magnetic fields. In both cases we further observed the coexistence of additional, secondary lattice-scale orders. This screening-induced tunability of broken-symmetry orders may prove valuable to uncover correlated phases of matter in other quantum materials.

Narrow electronic energy bands are exceptional playgrounds to explore many-body quantum phases of matter [1]. The vanishingly small kinetic energy in these narrow bands leaves electrons subjected to interaction effects alone, resulting in the emergence of a wealth of correlated, topological and broken-symmetry phases [2–6]. Nearly perfect flat-bands naturally develop in two-dimensional electron systems under a perpendicular magnetic field, B, as macroscopically-degenerate Landau levels in which interactions prevail. There, the main consequence of Coulomb interaction is to generate incompressible –gapped– phases at half integer filling of Landau levels, by favoring a spin-polarized ground state, a phenomenon called quantum Hall ferromagnetism [7].

In graphene, the additional valley degeneracy enriches the quantum Hall ferromagnetism with broken-symmetry states at every quarter filling [8, 9]. A central challenge in graphene is to unveil the nature of the ground state of the gapped zeroth Landau level (zLL) at charge neutrality. Theory predicts a rich phase diagram of broken-symmetry states with different topological properties [10–14]. While all are SU(4) ferromagnets, their exact spin and valley polarization (Fig. 1C) depends on a delicate balance between Zeeman energy and valley-anisotropy terms emerging from the lattice-scale interactions. Furthermore, the zLL wavefunctions feature a simple structure in which each valley degree of freedom is locked to one of the graphene's sublattices. This property isolates four possible broken-symmetry ground states that exhibit distinct sublattice or spin orders: a valley-polarized charge-density wave (CDW), a valley-polarized Kekulé bond (KB) order, a canted antiferromagnet (CAF) and a spin-polarized ferromagnet (F) (see Figs. 3A-C). Among them, the F order is a quantum Hall topological insulator harboring conducting helical edge states, while the rest are insulators with gapped edge states [15].

Experimentally, the main insights to distinguish different broken-symmetry ground states come from indirect transport measurements. High-mobility graphene devices typically show an unequivocal insulating behavior at charge neutrality upon increasing perpendicular magnetic field [9, 16–19]. On the other hand, a strong in-plane magnetic field that boosts the Zeeman effect and the ensuing spin-polarization can induce a transition to the helical phase with F order [20]. A recent alternative strategy utilized a high dielectric constant substrate to screen the long-range part of the Coulomb interaction [21]. This, in turn, enables the helical phase to emerge at moderate perpendicular magnetic fields, which eventually transits to a weak insulator upon increasing the magnetic field further. Such an apparent tunability of the broken-symmetry states between the helical and seemingly different insulating phases therefore suggests that a broad part of the phase diagram can be explored.

Here, we unambiguously identify three broken-symmetry states in the zLL of graphene by directly visualizing their lattice-scale order with scanning tunneling microscopy (STM) and spectroscopy. To access the different broken-symmetry states, we employed two different dielectric materials as substrate, both equipped with a back-gate electrode: the standard silicon oxide (SiO_2) and the quantum paraelectric strontium titanate oxide ($SrTiO_3$) with a remarkably high static dielectric constant of the order of $\epsilon_{STO} \approx 10^4$ at low tem-

* Corresponding author : benjamin.sacepe@neel.cnrs.fr

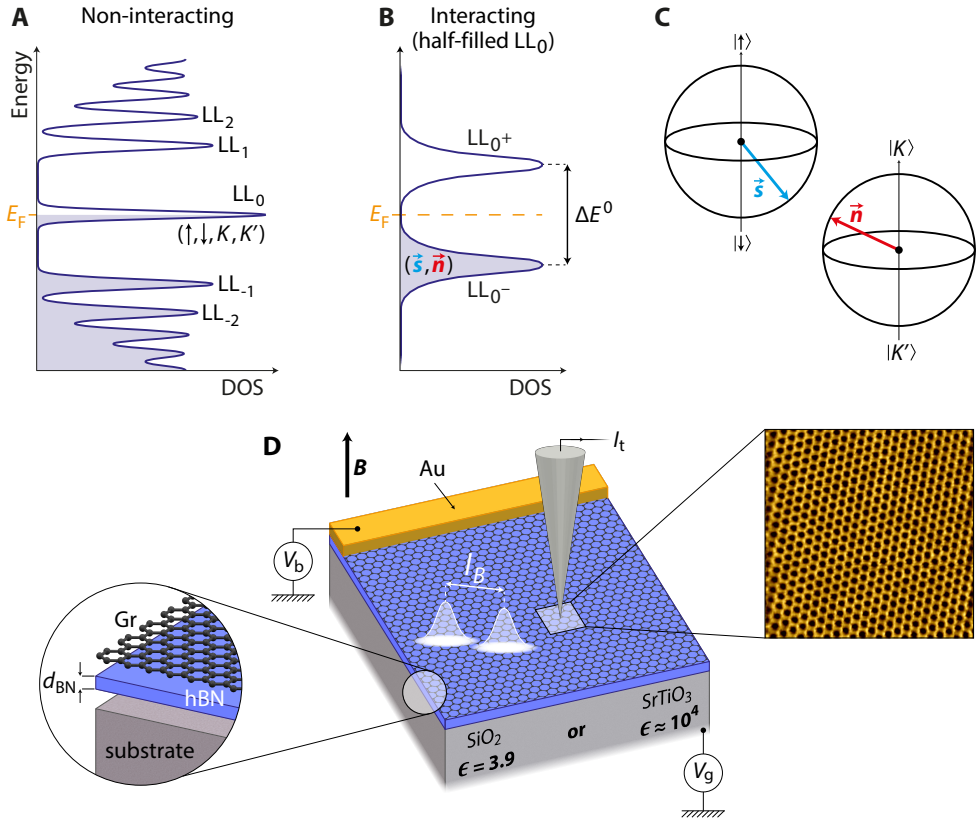

FIG. 1. **Landau level tunneling spectroscopy in graphene.** (**A**) Non-interacting density of states (DOS) of graphene under perpendicular magnetic field. Each Landau level (LL_N, N is the Landau level index) is spin $(\uparrow,\downarrow)$ and valley (K,K') degenerate and emerges as a peak separated from others by cyclotron gaps. (**B**) Due to exchange interaction, the half-filled LL_0 at charge neutrality splits into two peaks $\mathrm{LL}_{0\pm}$, thus opening an interaction-induced gap ΔE^0. The resulting broken-symmetry state features a SU(4)-polarization with a valley-polarization **n** and a spin-polarization **s** evolving in the SU(4) Bloch sphere constructed on the spin and valley subspaces, whose individual Bloch spheres are schematized in (**C**). (**D**) Schematics of the graphene samples. The two different substrates used are either SiO_2 (unscreened configuration) or the high-k dielectric $SrTiO_3$ (screened configuration). In both cases graphene is biased with the voltage V_b through an ohmic contact (in yellow) and its charge carrier density is tuned by the voltage V_g applied to a back-gate electrode. The tunneling current I_t is measured from the metallic tip. The tunneling spectroscopy is performed under perpendicular magnetic field B. The white disks on the sample illustrate the gaussian electronic wavefunction of LL_0 that extends on the scale of the magnetic length l_B. The left inset shows the graphene/hBN/substrate heterostructure, where d_BN is the hBN thickness. The right inset shows a $5\times5\,\mathrm{nm}^2$ STM image of the graphene honeycomb lattice measured on sample STO07 at 4 K and 0 T.

peratures (see SM). We fabricated samples consisting of monolayer graphene resting atop a thin hexagonal boron nitride (hBN) flake, deposited on the chosen substrate. To enable screening of the long-range Coulomb interaction [21], we selected hBN flakes (see SM) with thickness less than or of the order of the magnetic length $l_B = \sqrt{\hbar/eB}$ (where $\hbar$ is the reduced Planck constant and e is the electron charge) at low magnetic field, that is, the inter-electron distance in the zLL. Figure 1D displays a schematic of the sample structure, with a metallic contact on the graphene layer, which serves to bias the sample for tunneling measurements. All measurements were performed at a temperature of 4.2 K.

The Coulomb interaction strength can be readily assessed by tunneling spectroscopy [22] of the exchange gap that opens at half filling of the zLL (see Figs. 1A and B). Figure 2B displays a representative local tunneling conductance spectrum, $\mathrm{d}I_\mathrm{t}/\mathrm{d}V_\mathrm{b}$ versus V_b, measured on sample STO07 under a perpendicular magnetic field of 14 T. In this measurement, the Fermi level is adjusted at charge neutrality, that is, at half filling of the zLL, by applying a back-gate voltage $V_\mathrm{g} = 13$ V. While all Landau levels with index $|N| \geq 1$ appear in the tunneling conductance as sharp peaks separated by the cyclotron gap scaling as $\sqrt{|N|B}$ (see SM), the zLL splits into two peaks revealing the Coulomb gap of the $\nu = 0$ broken-symmetry state, ΔE^0, akin to earlier experiments in GaAs [23]. For accurate measurements of the gap, which reaches its maximum value at half-filling [7], we measured the back-gate dependence of the tunneling conductance as shown in Fig. 2A. The Landau level peaks in this color map form a staircase pattern, indicating the successive pinning of the Fermi level within each highly-degenerate Landau level [24, 25]. Analysis of individual

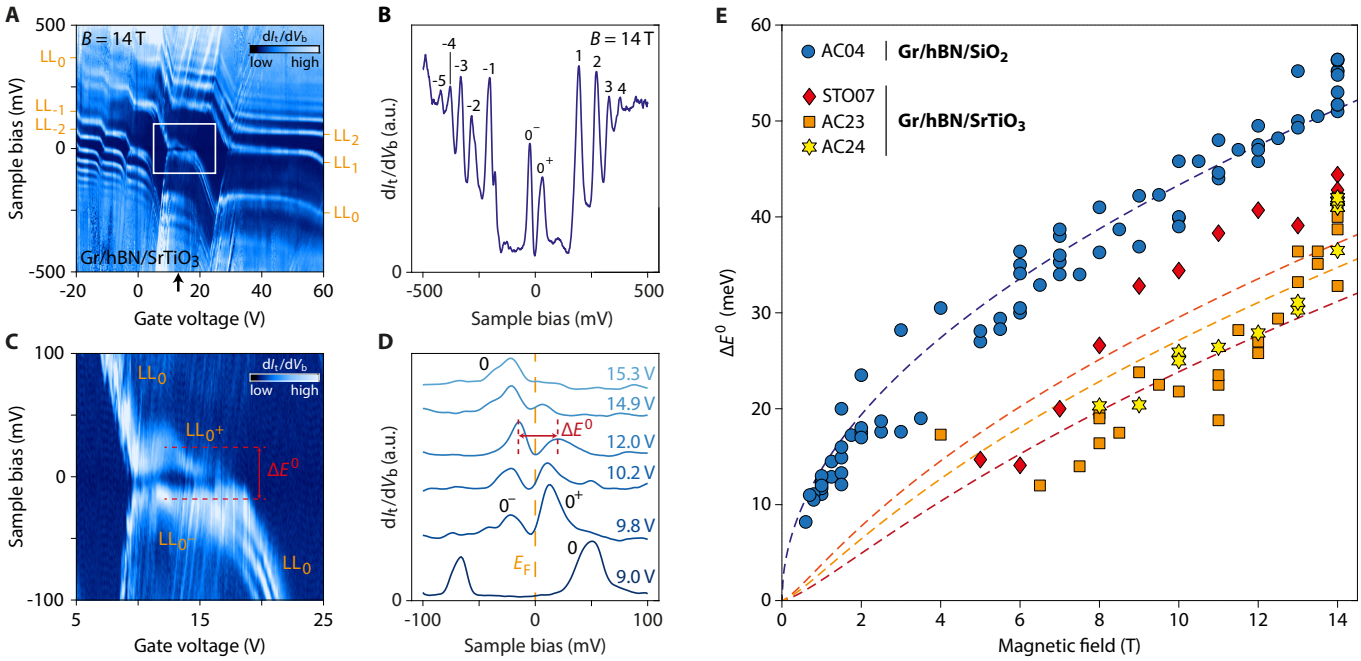

FIG. 2. **Quantum Hall ferromagnetic gap at charge neutrality.** (**A**) Local tunneling conductance gate map measured on graphene sample STO07 ($SrTiO_3$ substrate) at $B = 14$ T. The staircase pattern shows the successive pinning of the Fermi level E_F inside Landau levels. (**B**) Tunneling spectrum measured on the same sample at $B = 14$ T and $V_g = 13$ V, which corresponds to charge neutrality as indicated by the black arrow in (A). With E_F at half filling, the zLL splits into two peaks $LL_{0\pm}$ that defines the gap ΔE^0 of the broken-symmetry state. (**C**) Zoom of the white rectangle in (A) showing the splitting of the LL_0. (**D**) Spectra extracted from (C) at the back-gate voltages indicated on the right of each curve. (**E**) Evolution of ΔE^0 as a function of magnetic field for the four studied samples. For sample AC04 (SiO_2 substrate) the gap is fitted by the Coulomb energy $1/2\sqrt{\pi/2}\mathcal{E}_C \propto \sqrt{B}$ shown as a dashed blue line. For the three samples with $SrTiO_3$ substrates, ΔE^0 is decreased compared to sample AC04 due to the substrate screening of the Coulomb interaction. The red, orange and yellow dashed lines correspond to the substrate-screened Coulomb energy $\tilde{\mathcal{E}}_C$, computed with the respective hBN thickness of the samples.

spectra around charge neutrality thus enables us to evaluate ΔE^0, defined as the maximum separation between split peaks (see the red arrow in Figs. 2C and D).

Inspecting a systematic set of back-gate dependencies of the tunneling spectra for different magnetic field values, measured at various locations on the graphene surface, and on four different samples including SiO_2 and $SrTiO_3$ substrates (see SM), provides a robust determination of the B-dependence of the energy gap. Figure 2E displays the resulting values of ΔE^0 as a function of magnetic field.

We first focus on the unscreened case of sample AC04 (SiO_2 substrate) with the blue data points. A clear $\sqrt{B}$ dependence highlighted by the blue dashed line is observed starting at fields as low as 0.6 T and up to 14 T. This dependence reflects the growth of the Coulomb energy with B that scales as $\mathcal{E}_C = e^2/4\pi\epsilon_0\epsilon_r l_B \propto \sqrt{B}$, where ϵ_0 and ϵ_r are the vacuum permittivity and the relative permittivity surrounding the graphene. As the top graphene surface is exposed to vacuum, $\epsilon_r = (\epsilon_{BN} + 1)/2 \simeq 2.3$, where $\epsilon_{BN} \simeq 3.6$ is the hBN relative permittivity. Theoretically, ΔE^0 is expected to be $1/2\sqrt{\pi/2}\mathcal{E}_C$ [7]. We plot this quantity in Fig. 2E (blue dashed curve) by adjusting ϵ_r to 2.6, which is consistent with the expected value for the relative permittivity. Such a quantitative agreement with theory demonstrates the significance of our spectroscopy to assess the interaction-induced gap.

Remarkably, turning to the screened case with the $SrTiO_3$ substrate yields gap values conspicuously smaller than those obtained on the sample on SiO_2 (see red, orange and yellow data points in Fig. 2E). This reduction demonstrates, therefore, a clear screening of the Coulomb interaction by the high-dielectric constant of the substrate. Electrostatic considerations that account for the thin hBN bottom layer lead to a substrate-screened Coulomb energy scale $\tilde{\mathcal{E}}_C = \mathcal{E}_C \times S(B)$ that is mitigated by a screening factor $S(B) \approx 1 - \frac{\epsilon_{STO}-\epsilon_r}{\epsilon_{STO}+\epsilon_r}\frac{l_B}{\sqrt{l_B^2+4d_{BN}^2}}$, where d_{BN} is the hBN thickness [21]. Consequently, electrons in the graphene plane are subjected to an unusual B-dependent screening that depends on the ratio l_B/d_{BN} and is most efficient at low magnetic fields. In Fig. 2E the red, orange and yellow dashed curves show $\tilde{\mathcal{E}}_C$ calculated with the hBN thickness of the respective samples. Although the use of $\tilde{\mathcal{E}}_C$ is strictly valid only for hBN-encapsulated graphene, we obtain a decent agree-

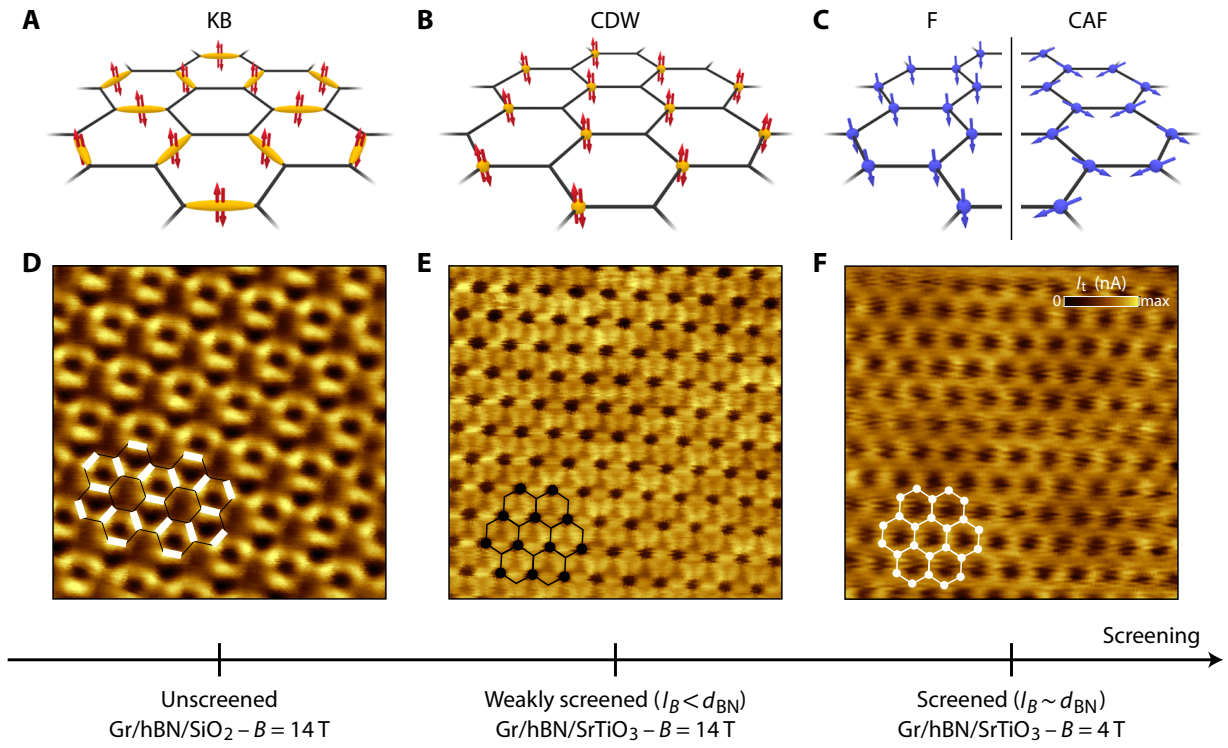

FIG. 3. **Tunable broken-symmetry states of charge-neutral graphene.** (**A-C**) Lattice-scale order drawings of the four possible broken-symmetry states in charge-neutral graphene under perpendicular magnetic field. (**A**) shows the Kekulé bond (KB) order, (**B**) the charge-density wave (CDW) with sublattice polarization and (**C**) the spin-polarized ferromagnetic (F) and canted anti-ferromagnetic (CAF) ground states. (**D-F**) 2.6×2.6 nm^2 STM images taken in constant height mode. (**D**) STM image on sample AC04 (unscreened graphene) at $B = 14$ T and $V_b = 25$ mV, which unveils a Kekulé bond order. (**E**) At $B = 14$ T (weakly-screened graphene, $l_B = 7$ nm $< d_{BN} = 12$ nm) and $V_b = 40$ mV, the sample AC23 exhibits a sublattice charge-density wave, whereas (**F**) at $B = 4$ T (screened graphene, $l_B = 13$ nm $\sim d_{BN} = 12$ nm) and $V_b = 20$ mV, we find a valley-unpolarized phase consistent with the spin-polarized helical phase. For each image we superposed a corresponding lattice drawing emphasizing the bond order, the sublattice polarization and the honeycomb lattice, respectively. The black horizontal arrow indicates the strength of substrate screening.

ment with our data, despite some scattering for sample STO07.

We now turn to the central result of this work, benchmarking the lattice-scale orders of the charge-neutral broken-symmetry state, upon tuning the screening of the Coulomb interaction. Figure 3 shows three STM images taken at the energy of a split zLL peak, on the SiO_2 sample AC04 at $B = 14$ T (Fig. 3D), and on the $SrTiO_3$ sample AC23 at $B = 14$ T (Fig. 3E) and 4 T (Fig. 3F). These panels thus cover three regimes for Coulomb interaction that we qualify as unscreened, moderately screened and screened, respectively. For the unscreened case in Fig. 3D, we observe a Kekulé distortion bond-order pattern of the electronic wavefunction, indicating that spin-singlet pairs of electrons are localized on one bond out of three per carbon atom of the graphene honeycomb lattice. This order is found to be stable down to $B = 3$ T (Fig. 4E). With the $SrTiO_3$ substrates at high magnetic field, that is, under moderate screening, another lattice-scale order develops with a stark valley-polarization: the CDW ground-state with the spin-singlet pairs now mostly localized on a single sublattice (Fig. 3E). This CDW order is found to be independent of the presence of a Moiré superlattice formed with the hBN layer (see SM). Finally, at low magnetic field (4T in Fig. 3F), this CDW order disappears, revealing a valley-unpolarized graphene honeycomb lattice, which points to a spin order.

Going further into the analysis of these ground states, we show below that additional fine structures emerge at the lattice scale, enriching the predicted phase diagram. The KB order features an unexpected, faint charge-density wave that has the periodicity of the Kekulé unit cell. This coexisting order is readily seen in Fig. 4A : a nicely formed Kekulé pattern exhibits an enhanced local wavefunction amplitude inside one hexagon of the honeycomb that repeats periodically on the Kekulé triangular lattice, as indicated by the blue circles and dashed lines in Fig. 4B. Figure 4C provides an overall representation of the latter superimposed on the honeycomb and Kekulé lattices. This new charge-density wave that we label as K-CDW, is different from the CDW broken-symmetry state since it displays a triangular lattice with a parameter $\sqrt{3}$ times larger than the graphene lattice parame-

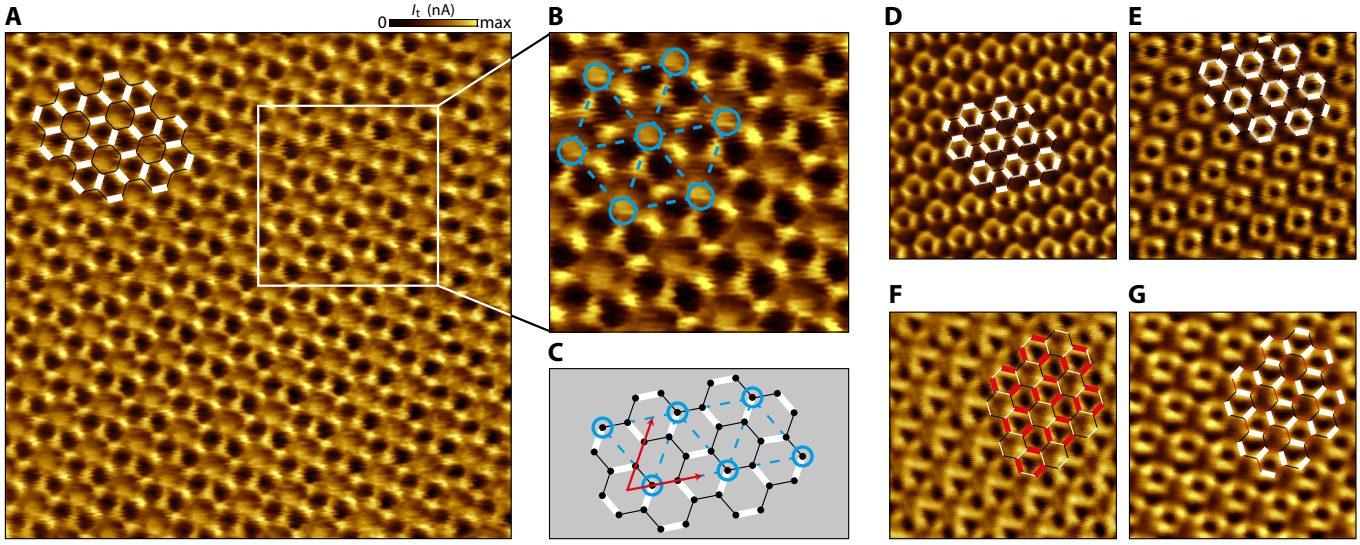

FIG. 4. **Kekulé bond order in unscreened charge-neutral graphene.** (**A**) $5 \times 5\,\mathrm{nm}^2$ STM image on sample AC04, at $B = 14\,\mathrm{T}$ and $V_\mathrm{b} = 25\,\mathrm{mV}$. The KB lattice, where both electrons of the broken-symmetry state are localized on one C-C bond out of three, is shown in overlay with the stronger bonds highlighted in thick white. This structure is detailed in (**C**) where the basis vectors of the KB order lattice are indicated in red. A zoom of (A) is displayed in (**B**), where we observe a secondary, long-range charge-density-wave order featuring a triangular lattice (drawn in blue) with a parameter matching the one of the Kekulé lattice ($\sqrt{3}$ times the graphene lattice parameter). (**D, E**) $3 \times 3\,\mathrm{nm}^2$ images showing asymmetric Kekulé patterns. (D) At $B = 14\,\mathrm{T}$ and $V_\mathrm{b} = 2\,\mathrm{mV}$ the three Kekulé strong bonds are partially merged, while in (E) at $B = 3\,\mathrm{T}$ and $V_\mathrm{b} = 30\,\mathrm{mV}$ they are completely merged and form a circle-like overall pattern. (**F, G**) $3 \times 3\,\mathrm{nm}^2$ images at $B = 14\,\mathrm{T}$, at $V_\mathrm{b} = 25\,\mathrm{meV}$ acquired at the same position a few minutes apart, showing the transition between two degenerate Kekulé configurations from the red Kekulé lattice in (F) to the white one in (G). Both lattices in overlay are at the same position. All images are taken in constant height mode.

ter. The tripled unit cell of the K-CDW is reminiscent of CDW phases observed to compete with the Kekulé order in extended Hubbard-models at $B = 0$ [26–29], but have not been reported or predicted at finite B. We also observed other situations in which this K-CDW induces a pronounced asymmetry of the Kekulé pattern, with a more or less merging of the Kekulé strong bonds (see SM). This is illustrated by the evolution from the mostly symmetric Kekulé lattice shown in Fig. 4A to the pronounced asymmetric Kekulé lattices shown in Figs. 4D and E. If on some images the strong bonds are still visible (see Fig. 4D), they can also merge with each other, forming a circle-like pattern seen in Fig. 4E. Note that both the KB order and the underlying K-CDW disappear when the bias voltage is away from the zLL peaks (see SM), which rules out a tip-induced artifact as the origin of the observed KB order.

Interestingly, both the KB order and K-CDW vary with time. For instance, Figs. 4F and G show a spontaneous transition from one of the three possible degenerate Kekulé lattices to another, while imaging continuously the very same location. Similar changes for the K-CDW are shown in SM.

In screened graphene, likewise, close inspection of the CDW broken-symmetry state reveals striking fine structures. In the following we assume that the electron doublets of the CDW are localized on the sublattice A (in blue), while the sublattice B is empty (in red) as represented in the inset of Fig. 5A. We start by deciphering Figs. 5B and C, taken at the exact same location, and comparing the occupied and empty orbitals of the exact same atoms. In both images the CDW appears as dark spots featuring a triangular symmetry and corresponding to the atoms of a single sublattice (the sublattice B in Fig. 5B and the sublattice A in Fig. 5C), whereas atoms of the other sublattice are not visible. Extracting electrons from the occupied states into the STM tip at negative sample bias leads to a very low tunneling current on the empty atoms of the sublattice B (dark spots in Fig. 5B). Similarly, injecting electrons from the STM tip into the empty states at positive sample bias leads to a very low current on the already doubly occupied atoms of the sublattice A (dark spots in Fig. 5C).

In addition, inspecting Fig. 5C, we see that atoms of sublattice B (red spots in the inset) are located in the middle of a triangular lattice formed by bright lines joining the doubly-occupied atoms of the sublattice A, which correspond to high density of empty states. One can also notice in Fig. 5C that the triangular cells that contain atoms B are brighter than the other empty cells, which is consistent with the enhancement of the local density of empty states by the B atoms. We illustrate this unusual sublattice inversion with the lattice drawings in Figs. 5G and H, where the density of occupied and emptied states

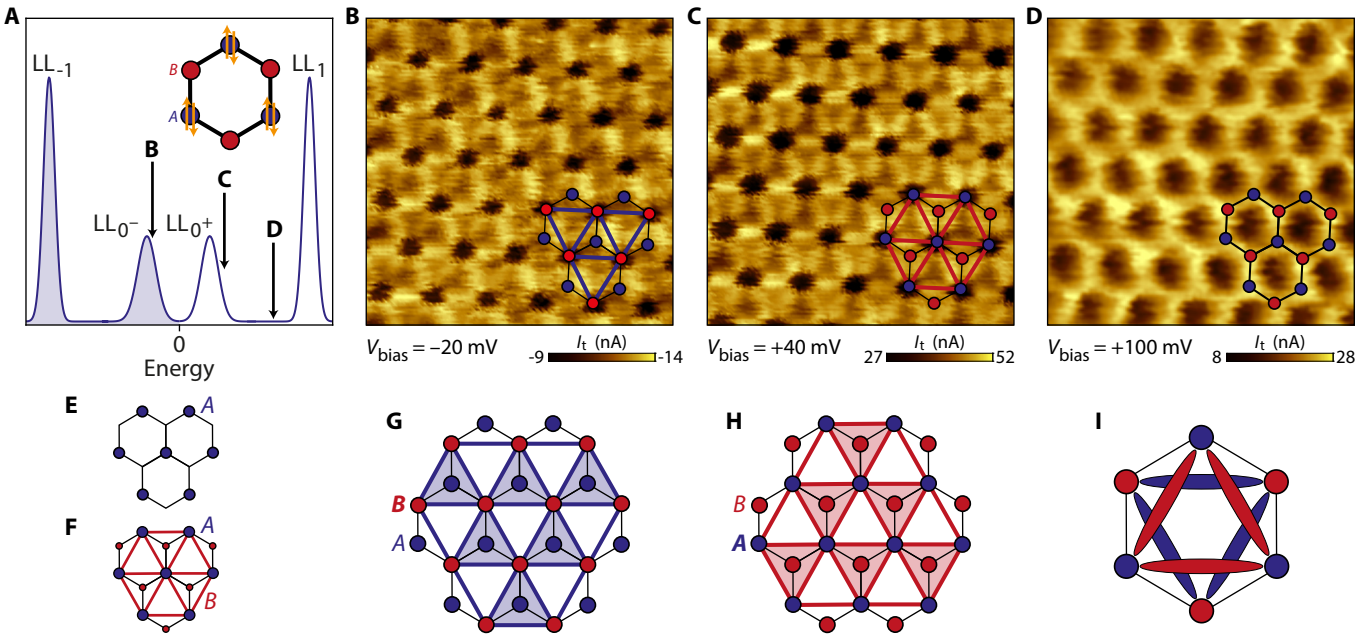

FIG. 5. **Charge-density-wave order in moderately screened charge-neutral graphene.** (**A**) Simulated Landau spectrum indicating the bias voltage positions of the subsequent $1.5 \times 1.5\ \mathrm{nm}^2$ constant-height STM images, all acquired at $B = 14$ T and at the same location on sample AC23. Inset: Convention for the CDW lattice, the blue sublattice A is doubly occupied whereas the red sublattice B is empty. (**B**) Image at $V_\mathrm{b} = -20$ mV with the CDW lattice in overlay: the sublattice B (empty) appears as dark spots at negative bias and intra-sublattice bonds are visible as bright lines between them. (**C**) Similarly, at the positive bias of $V_\mathrm{b} = +40$ mV, the sublattice A (doubly occupied) appears as dark spots and intra-sublattice bonds are visible as bright lines between them. Note that the colorscale in (B) is inverted with respect to that in (C), since the tunneling current is negative due to the negative bias. (**D**) At $V_\mathrm{b} = 100$ mV, the CDW is no longer visible and the honeycomb lattice appears instead. (**E**) CDW with full sublattice polarization, as predicted in Ref. [14], compared to a CDW with partial sublattice polarization in (**F**). The symmetry-allowed triangular bond order is suppressed in (E), and coexists with the CDW in (F), where a triangular lattice emerges due to a symmetry allowed sublattice hopping-asymmetry. In (F) the difference in size for the A and B atoms represents the partial sublattice polarization. (**G,H**) Sketch showing the CDW sublattice inversion between negative bias in (G) and positive bias in (H). (**I**) Structure of the intra-sublattice bonds.

are color coded blue and red, respectively. Figure 5I summarizes this remarkable inverted pattern by superposing the empty (red) and occupied (blue) states on the same carbon hexagon.

This additional triangular order that accompanies the CDW in Fig. 5 was not expected in the theory of charge-neutral graphene [14]. Such a sublattice bond asymmetry, $t_{2,A} \neq t_{2,B}$ ($t_{2,A}$ and $t_{2,B}$ are the second-nearest-neighbor bond expectation values of sublattices A and B, respectively), is generically permitted in the CDW phase as it gaps out the zLL with the same matrix structure as a sublattice charge imbalance [30] (see SM). It becomes visible when the sublattice degree of freedom is partially polarized (see Figs. 5E and F). We conjecture that this partial sublattice polarization could originate from Landau level mixing, since the sublattice index is decoupled from valley index in higher Landau levels [31–33].

The observation of these three ground states has profound implications for the understanding of transport properties at charge neutrality. For the unscreened case, corresponding to virtually all transport experiments, the KB order is in contradiction with the transition scenario from the conjectured CAF phase to the helical F phase tuned by the Zeeman field [14, 20], as well as with recent magnon transmission experiments [34–37] that imply magnetism. Note that a KB order has also been observed in graphene multilayers [38]. Nonetheless, a recent prediction [33] suggests that both KB order and CAF phases could co-exist, thus accounting for the experimental dissonance. Our observation of a sub-dominant K-CDW order adds yet a new flavor to the phase diagram, which was not anticipated thus far and deserves further theoretical attention. Similarly, the nature of edge excitations may be more complex than initially thought [39]. A definitive conclusion on the existence of an underlying magnetism in this ground state and its possible spin texture at the lattice scale (Fig. 3C) would require further spin-filtered scanning tunneling experiments, beyond the scope of this work.

Furthermore, our observation of coexisting orders implies that the nature of bulk excitations in this insulating phase must be revisited [40]. The time-varying nature of the KB order and K-CDW, indicating some depinning mechanisms and the presence of domain walls, may indeed give a relevant contribution to charge transport, in parallel to skyrmion excitations. A Kosterlitz-

Thouless phase transition driven by topological Kekulé vortex zero-modes [41] has been indeed predicted [42] and discussed experimentally [18, 19].

In the screened case, we observed the CDW persisting from $B = 14\,\mathrm{T}$ down to $B = 7\,\mathrm{T}$ (see SM) and disappearing at $B = 4\,\mathrm{T}$ in favour of a valley-unpolarized phase at lower magnetic field. This phase transition is consistent with the spin-polarized helical phase observed in transport measurements [21], which is replaced by a weakly insulating phase at high fields, corresponding to the CDW phase unveiled in this work. The scenario explaining the change of ground state due to substrate screening was accounted for by a modification of renormalization effects of the valley-anisotropy energies by the (screened) long-range Coulomb interaction. Although it is difficult to assess this renormalization experimentally, the substrate screening of the Coulomb interaction evidenced by our spectroscopy of the zLL gap indicates that such a mechanism is likely to be at play. As the screening exhibits an unusual, inversely proportional B-dependence, our findings, supported by the transport experiments, therefore confirm a modification of the valley-anisotropy energies upon varying the magnetic field in this specific substrate-screened configuration.

Ultimately, at much higher fields such that $l_B \ll d_{BN}$, one should expect in graphene samples on $SrTiO_3$ another transition from the CDW to the KB phase. In this situation the substrate screening vanishes and the Coulomb energy scale asymptotically reaches its bare value.

In conclusion, our work deciphers the phase diagram of a many-body interacting system: quantum Hall ferromagnetism of charge-neutral graphene. We showed how to tune between different broken-symmetry states, clearly demonstrating the profound impact that the screening of the long-range Coulomb interaction can have. Furthermore, the unexpected occurrence of coexisting secondary orders as well as their time-varying nature underlines the complexity of the true phase diagram and incites further investigation.

Note: Another very recent work (https://arxiv.org/abs/2109.11555) that appeared during the writing of our manuscript also reports the observation of the Kekulé phase in the unscreened configuration.

DATA AVAILABILITY

The data that support the findings of this study are available from the corresponding author upon reasonable request.

ACKNOWLEDGMENTS

We thank F. de Juan, H. Fertig, M. Goerbig, G. Murthy and E. Shimshoni for valuable discussions. We thank B. Kousar for careful reading of the manuscript. We thank D. Dufeu, D. Grand, D. Lepoittevin and P. Plaindoux for technical support in the setup of the experimental apparatus. Samples were prepared at the Nanofab facility of the Néel Institute. This work has received funding from the European Union's Horizon 2020 research and innovation program ERC grants *QUEST* No. 637815 and *SUPERGRAPH* No. 866365, and the Marie Sklodowska-Curie grant QUESTech No. 766025. A. G. G. acknowledges financial support by the ANR under the grant ANR-18-CE30-0001-01 (TOPODRIVE).

COMPETING INTERESTS

The authors declare that they have no competing financial interests.

[1] Hubbard, J. Electron correlations in narrow energy bands. *Proc. R. Soc. Lond. A* **276**, 238–257 (1963).

[2] Cao, Y. *et al.* Unconventional superconductivity in magic-angle graphene superlattices. *Nature* **556**, 43–50 (2018).

[3] Cao, Y. *et al.* Correlated insulator behaviour at half-filling in magic-angle graphene superlattices. *Nature* **556**, 80–84 (2018).

[4] Wong, D. *et al.* Cascade of electronic transitions in magic-angle twisted bilayer graphene. *Nature* **582**, 198–202 (2020).

[5] Zondiner, U. *et al.* Cascade of phase transitions and Dirac revivals in magic-angle graphene. *Nature* **582**, 203–208 (2020).

[6] Saito, Y. *et al.* Hofstadter subband ferromagnetism and symmetry-broken Chern insulators in twisted bilayer graphene. *Nature Physics* **17**, 478–781 (2021).

[7] Ezawa, Z. F. *Quantum Hall Effects* (World Scientific Publishing, 2013).

[8] Nomura, K. & MacDonald, A. H. Quantum Hall Ferromagnetism in Graphene. *Phys. Rev. Lett.* **96**, 256602 (2006).

[9] Young, A. F. *et al.* Spin and valley quantum Hall ferromagnetism in graphene. *Nature Physics* **8**, 550 (2012).

[10] Alicea, J. & Fisher, M. P. A. Graphene integer quantum Hall effect in the ferromagnetic and paramagnetic regimes. *Phys. Rev. B* **74**, 075422 (2006).

[11] Herbut, I. F. Theory of integer quantum Hall effect in graphene. *Phys. Rev. B* **75**, 165411 (2007).

[12] Herbut, I. F. SO(3) symmetry between Néel and ferromagnetic order parameters for graphene in a magnetic field. *Phys. Rev. B* **76**, 085432 (2007).

[13] Jung, J. & MacDonald, A. H. Theory of the magnetic-field-induced insulator in neutral graphene sheets. *Phys. Rev. B* **80**, 235417 (2009).

[14] Kharitonov, M. Phase diagram for the $\nu = 0$ quantum Hall state in monolayer graphene. *Phys. Rev. B* **85**, 155439 (2012).

[15] Kharitonov, M., Juergens, S. & Trauzettel, B. Interplay of topology and interactions in quantum Hall topological insulators: U(1) symmetry, tunable Luttinger liquid, and interaction-induced phase transitions. *Phys. Rev. B* **94**, 035146 (2016).

[16] Zhang, Y. *et al.* Landau-Level Splitting in Graphene in High Magnetic Fields. *Phys. Rev. Lett.* **96**, 136806 (2006).

[17] Abanin, D. A. *et al.* Dissipative Quantum Hall Effect in Graphene near the Dirac Point. *Phys. Rev. Lett.* **98**, 196806 (2007).

[18] Checkelsky, J. G., Li, L. & Ong, N. P. Zero-Energy State in Graphene in a High Magnetic Field. *Phys. Rev. Lett.* **100**, 206801 (2008).

[19] Checkelsky, J. G., Li, L. & Ong, N. P. Divergent resistance at the Dirac point in graphene: Evidence for a transition in a high magnetic field. *Phys. Rev. B* **79**, 115434 (2009).

[20] Young, A. F. *et al.* Tunable symmetry breaking and helical edge transport in a graphene quantum spin Hall state. *Nature* **505**, 528–532 (2014).

[21] Veyrat, L. *et al.* Helical quantum Hall phase in graphene on $SrTiO_3$. *Science* **367**, 781–786 (2020).

[22] Andrei, E. Y., Li, G. & Du, X. Electronic properties of graphene: a perspective from scanning tunneling microscopy and magnetotransport. *Rep. Prog. Phys.* **75**, 056501 (2012).

[23] Dial, O. E., Ashoori, R. C., Pfeiffer, L. N. & West, K. W. High-resolution spectroscopy of two-dimensional electron systems. *Nature* **448**, 176–179 (2007).

[24] Luican, A., Li, G. & Andrei, E. Y. Quantized Landau level spectrum and its density dependence in graphene. *Phys. Rev. B* **83**, 041405(R) (2011).

[25] Chae, J. *et al.* Renormalization of the Graphene Dispersion Velocity Determined from Scanning Tunneling Sprectroscopy. *Phys. Rev. Lett.* **109**, 116802 (2012).

[26] Grushin, A. G. *et al.* Charge instabilities and topological phases in the extended Hubbard model on the honeycomb lattice with enlarged unit cell. *Phys. Rev. B* **87**, 085136 (2013).

[27] García-Martínez, N. A., Grushin, A. G., Neupert, T., Valenzuela, B. & Castro, E. V. Interaction-driven phases in the half-filled spinless honeycomb lattice from exact diagonalization. *Phys. Rev. B* **88**, 245123 (2013).

[28] Motruk, J., Grushin, A. G., de Juan, F. & Pollmann, F. Interaction-driven phases in the half-filled honeycomb lattice: An infinite density matrix renormalization group study. *Phys. Rev. B* **92**, 085147 (2015).

[29] Capponi, S. & Läuchli, A. M. Phase diagram of interacting spinless fermions on the honeycomb lattice: A comprehensive exact diagonalization study. *Phys. Rev. B* **92**, 085146 (2015).

[30] Alba, E., Fernandez-Gonzalvo, X., Mur-Petit, J., Pachos, J. K. & Garcia-Ripoll, J. J. Seeing Topological Order in Time-of-Flight Measurements. *Physical Review Letters* **107**, 235301 (2011).

[31] Peterson, M. R. & Nayak, C. Effects of Landau Level Mixing on the Fractional Quantum Hall Effect in Monolayer Graphene. *Phys. Rev. Lett.* **113**, 086401 (2014).

[32] Feshami, B. & Fertig, H. A. Hartree-Fock study of the $\nu = 0$ quantum Hall state of monolayer graphene with short-range interactions. *Physical Review B* **94** (2016).

[33] Das, A., Kaul, R. K. & Murthy, G. Coexistence of Canted Antiferromagnetism and Bond-order in $\nu = 0$ Graphene. *arXiv*:2109.07515 (2021).

[34] Takei, S., Yacobi, A., Halperin, B. I. & Tserkovnyak, Y. Spin Superfluidity in the $\nu = 0$ Quantum Hall State of Graphene. *Phys. Rev. Lett.* **116**, 216801 (2016).

[35] Wei, D. S. *et al.* Electrical generation and detection of spin waves in a quantum Hall ferromagnet. *Science* **362**, 229–233 (2018).

[36] Stepanov, P. *et al.* Long-distance spin transport through a graphene quantum Hall antiferromagnet. *Nature Physics* **14**, 907–911 (2018).

[37] Assouline, A. *et al.* Unveiling excitonic properties of magnons in a quantum Hall ferromagnet. *arXiv*:2102.02068 (2021).

[38] Li, S.-Y., Zhang, Y., Yin, L.-J. & He, L. Scanning tunneling microscope study of quantum Hall isospin ferromagnetic states in the zero Landau level in a graphene monolayer. *Phys. Rev. B* **100**, 085437 (2019).

[39] Knothe, A. & Jolicoeur, T. Edge structure of graphene monolayers in the $\nu = 0$ quantum Hall state. *Phys. Rev. B* **92**, 165110 (2015).

[40] Atteia, J., Lian, Y. & Goerbig, M. O. Skyrmion zoo in graphene at charge neutrality in a strong magnetic field. *Phys. Rev. B* **103**, 035403 (2021).

[41] Hou, C.-Y., Chamon, C. & Mudry, C. Electron Fractionalization in Two-Dimensional Graphenelike Structures. *Phys. Rev. Lett.* **98**, 186809 (2007).

[42] Nomura, K., Ryu, S. & Lee, D.-H. Field-Induced Kosterlitz-Thouless Transition in the $N = 0$ Landau Level of Graphene. *Phys. Rev. Lett.* **103**, 216801 (2009).

[43] Wang, L. *et al.* One-Dimensional Electrical Contact to a Two-Dimensional Material. *Science* **342**, 614–617 (2013).

[44] Li, X.-X. *et al.* Gate-controlled reversible rectifying behaviour in tunnel contacted atomically-thin MoS_2 transistor. *Nature Communications* **8**, 970 (2017).

[45] Choi, Y. *et al.* Electronic correlations in twisted bilayer graphene near the magic angle. *Nature Physics* **15**, 1174–1180 (2019).

[46] Grupp, D. E. & Goldman, A. M. Giant Piezoelectric Effect in Strontium Titanate at Cryogenic Temperatures. *Science* **276**, 392–394 (1997).

[47] Honig, M. *et al.* Local electrostatic imaging of striped domain order in $LaAlO_3/SrTiO_3$. *Nature Materials* **12**, 1112–1118 (2013).

[48] Sakudo, T. & Unoki, H. Dielectric Properties of $SrTiO_3$ at Low Temperatures. *Phys. Rev. Lett.* **26**, 851–853 (1971).

[49] Hemberger, J., Lunkenheimer, P., Viana, R., Böhmer, R. & Loidl, A. Electric-field-dependent dielectric constant and nonlinear susceptibility in $SrTiO_3$. *Phys. Rev. B* **52**, 13159 (1995).

[50] Sachs, R., Lin, Z. & Shi, J. Ferroelectric-like $SrTiO_3$ surface dipoles probed by graphene. *Scientific Reports* **4**, 3657 (2014).

[51] Chen, S., Chen, X., Duijnstee, E. A., Sanyal, B. & Banerjee, T. Unveiling Temperature-Induced Structural Domains and Movement of Oxygen Vacancies in $SrTiO_3$ with Graphene. *ACS Appl. Mater. Interfaces* **12**, 52915–52921 (2020).

[52] Das Sarma, S., Hwang, E. H. & Tse, W.-K. Many-body interaction effects in doped and undoped graphene: Fermi liquid versus non-fermi liquid. *Phys. Rev. B* **75**, 121406(R) (2007).

[53] Gutiérrez, C. *et al.* Interaction-driven quantum Hall wedding cake-like structures in graphene quantum dots. *Sci-*

ence **361**, 789–794 (2018).

[54] Luican-Mayer, A. *et al.* Screening Charged Impurities and Lifting the Orbital Degeneracy in Graphene by Populating Landau levels. *Phys. Rev. Lett.* **112**, 036804 (2014).

[55] Groth, C. W., Wimmer, M., Akhmerov, A. R. & Waintal, X. Kwant: a software package for quantum transport. *New Journal of Physics* **16**, 063065 (2014).

[56] Hauschild, J. & Pollmann, F. Efficient numerical simulations with Tensor Networks: Tensor Network Python (TeNPy). *SciPost Phys. Lect. Notes* 5 (2018).

Supplementary Materials

I. SAMPLE FABRICATION

Graphene/hBN heterostructures were assembled from exfoliated flakes with the van der Waals pick-up technique using a polypropylene carbonate (PPC) polymer [43]. Stacks were deposited using the methods described in Ref. [44] (for sample STO07) or in Ref. [45] (for samples AC04, AC23 and AC24), on either highly doped Si wafers with a 285 nm thick SiO_2 layer or on, 500 μm thick, $SrTiO_3$ [100] substrates that were cleaned with hydrofluoric acid buffer solution before deposition of the graphene/hBN heterostructures (a Ti/Au bilayer was deposited later on the other side of the $SrTiO_3$ substrate to enable back-gate effect). Electron-beam lithography using a PMMA resist was used to pattern a guiding markerfield on the whole $5 \times 5\,\mathrm{mm}^2$ substrate to drive the STM tip toward the device. Cr/Au electrodes contacting the graphene flake were also patterned by electron-beam lithography and metalized by e-gun evaporation. Samples were thermally annealed at 350 °C in vacuum under an halogen lamp to remove resist residues and clean graphene, before being mounted into the STM where they were heated *in situ* during the cooling to 4.2 K.

II. MEASUREMENTS

Experiments were performed with a home-made hybrid scanning tunneling microscope (STM) and atomic force microscope (AFM) operating at a temperature of 4.2 K in magnetic fields up to 14 T. The AFM mode is used to guide the tip toward the graphene device. The sensor consists of a hand-cut PtIr tip glued on the free prong of a tuning fork, the other prong being glued on a Macor substrate. Once mounted inside the STM, the tip is roughly aligned over the sample at room temperature and then guided toward the graphene device in AFM mode at low temperature using the guiding markerfield on the sample. Scanning tunneling spectroscopy (STS) was performed using a lock-in amplifier technique with a modulation frequency of 263 Hz and rms modulation voltage between $1 - 5$ mV depending on the spectral range of interest.

Differential conductance, $\mathrm{d}I_\mathrm{t}/\mathrm{d}V_\mathrm{b}$, gate maps were obtained by measuring tunneling spectra as the back-gate voltage V_g is swept at fixed tip position. For samples on SiO_2, we measured directly the $\mathrm{d}I_\mathrm{t}/\mathrm{d}V_\mathrm{b}$ tunneling spectra as the back-gate voltage V_g was swept continuously. For samples on $SrTiO_3$, due to the strong piezoelectric effect of the substrate [46, 47], we maintained the back-gate voltage constant during each sample bias sweep to avoid changes of the tunneling conductance caused by expansion or shrinkage of the substrate, leading to diverging or vanishing tunneling current respectively. The $\mathrm{d}I_\mathrm{t}/\mathrm{d}V_\mathrm{b}$ gate map measurements on $SrTiO_3$ were also systematically carried out by maintaining the same back-gate voltage sweep limits in order to compensate for the dielectric hysteresis of the substrate and to maintain the position of the charge-neutrality point at the same back-gate voltage.

Imaging of charge-neutral graphene ground states were done in STM constant-height mode. Starting from tunneling contact at ($V_\mathrm{b} = 300\,\mathrm{mV}$, $I_\mathrm{t} = 1\,\mathrm{nA}$) with the Z-regulation on, we switch off the regulation and lower the bias voltage to energies corresponding to the $\mathrm{LL}_{0^\pm}$ peaks, which drastically decreases the tunneling current. We then manually approach the tip toward graphene until we restore a tunneling current of a few nA. STM scans with atomic resolution are subsequently realized to image the honeycomb lattice or its eventual polarization into one of the four possible ground states.

III. SAMPLES SUMMARY

We studied two different types of samples (see Fig. 1D of the main text) : first graphene on hBN/SiO_2 substrate, the usual substrate used in transport measurements, and secondly graphene on hBN/$SrTiO_3$ substrate with a thin hBN layer of thickness d_{BN} (see Table I). Optical images of the samples are shown in Fig. S1 and their geometrical parameters are listed in Table I. Both types of samples are equipped with a back-gate electrode.

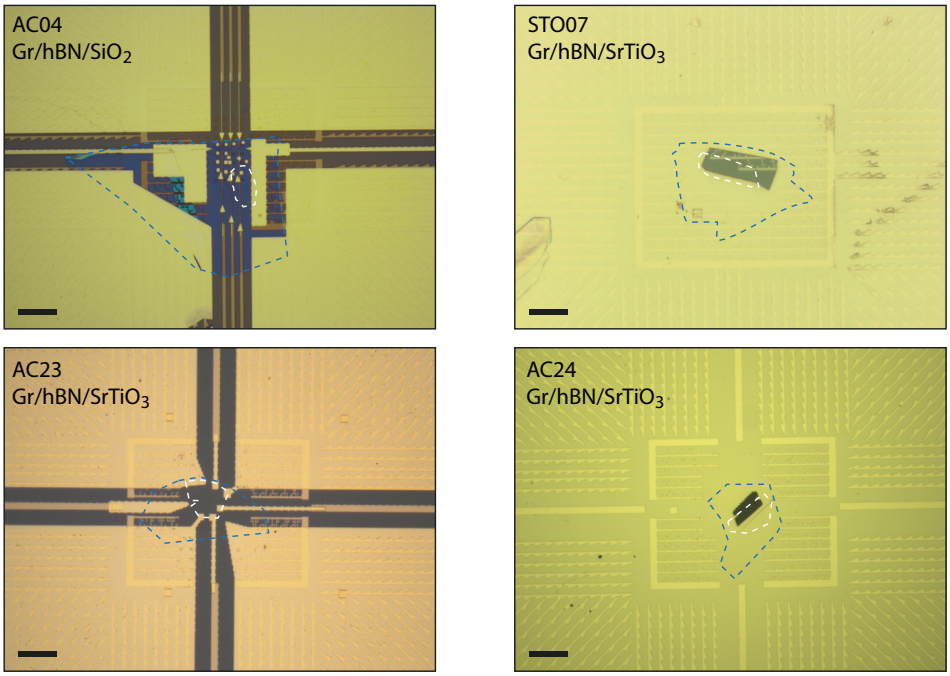

FIG. S1. **Graphene samples.** Optical pictures of the studied samples listed in Table I. The dashed blue lines outline the hBN flakes, while the white dashed lines outline the graphene flakes. For every image, the scale bar is 10 μm.

Sample	AC04	STO07	AC23	AC24
Substrate	Si^{++}/SiO_2	$SrTiO_3$	$SrTiO_3$	$SrTiO_3$
Substrate/oxide thickness	285 nm	500 μm	500 μm	500 μm
hBN thickness (d_{BN})	14 nm	8 nm	12 nm	10 nm

TABLE I. Geometrical parameters of the four measured samples.

IV. ESTIMATION OF THE DIELECTRIC CONSTANT OF $SrTiO_3$ IN MAGNETIC FIELD

We show in this section how we can estimate the $SrTiO_3$ dielectric constant, ϵ_{STO}, from tunneling conductance gate maps. ϵ_{STO} is linked to the global dielectric constant of the back gate, ϵ_r, which can be obtained by modeling the back-gate capacitance C_g as the sum of the series capacitances of $SrTiO_3$ and hBN assuming plane capacitors :

$$\frac{1}{C_g} = \frac{1}{C_{STO}} + \frac{1}{C_{BN}} \Rightarrow \frac{d_{STO} + d_{BN}}{\epsilon_r} = \frac{d_{STO}}{\epsilon_{STO}} + \frac{d_{BN}}{\epsilon_{BN}} \tag{1}$$

Since $d_{BN} \sim 10\,\text{nm} \ll d_{STO} = 500\,\mu\text{m}$, we write the gate insulator dielectric constant as :

$$\epsilon_r = \epsilon_{STO}\left(1 + \frac{d_{BN}}{d_{STO}}\frac{\epsilon_{STO}}{\epsilon_{BN}}\right)^{-1} \tag{2}$$

Numerically, $\epsilon_{BN} \simeq 3.6$ and $\epsilon_{STO} \sim 10^4$ at low temperature [48], so that $d_{BN}\epsilon_{STO}/d_{STO}\epsilon_{BN} \sim 0.1$. We can assume that $\epsilon_r \simeq \epsilon_{STO}$: the back-gate insulator capacitance is thus mainly determined by the dielectric constant of $SrTiO_3$.

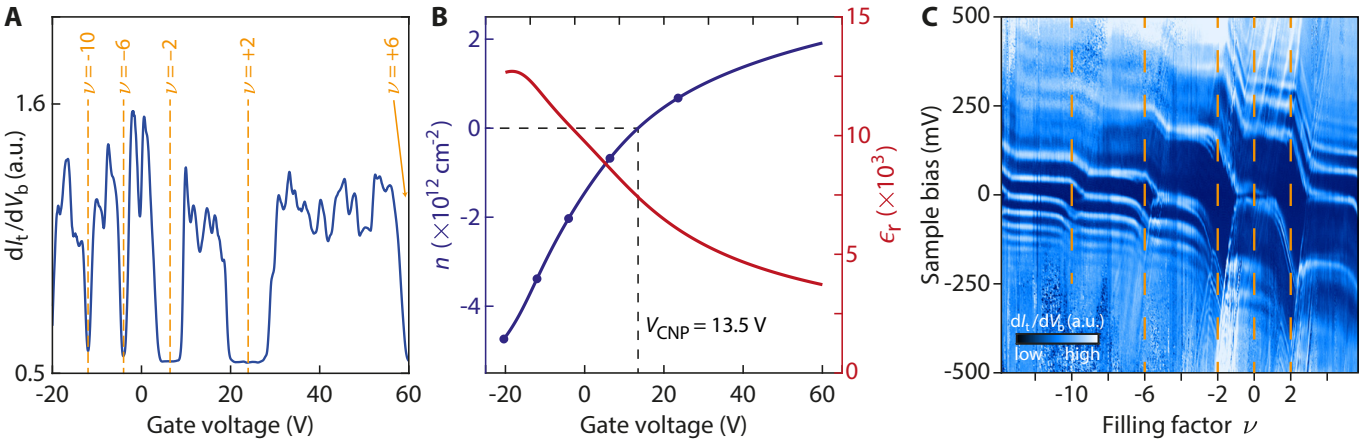

FIG. S2. **Estimation of the dielectric constant of $SrTiO_3$ and rescaling of the gate map.** (**A**) Line cut at $V_b = 0$ V, averaged on a range of ± 20 mV, of the dI_t/dV_b gate map at $B = 14$ T in Fig. 2A of the main text, which gives back-gate voltages corresponding to filling factors ν of filled LLs. (**B**) Estimation from the filling factors obtained in (A) of the charge carrier density n (blue dots), polynomial fit (blue curve) and computed values of $\epsilon_r \simeq \epsilon_{STO}$ as a function of gate voltage. The fit also yields $V^{CNP} \simeq 13.5$ V. (**C**) Rescaling of the gate map as a function of ν.

In order to estimate ϵ_r as a function of the back-gate voltage, we consider the tunneling conductance gate map at $B = 14$ T from Fig. 2A of the main text (sample STO07) from which we can extract some values of the back-gate voltage at specific filling factors ν. Furthermore, note that the electron-hole asymmetry visible in this gate map stems from the non-linear behavior of ϵ_{STO} with the gate voltage [21, 49–51]. Since the successive plateaus that form in the gate map correspond to the filling of LLs, the variation of gate voltage to pass through an entire plateau yields a variation in terms of filling factor of $\Delta\nu = \pm 4$. We plot in Fig. S2A the line cut of the gate map at zero bias, averaged on a range of ± 20 meV around this value. We clearly observe the different non-zero conductance plateaus forming when E_F is pinned inside one LL, with gaps in-between. We next consider that the gate voltages at the middle of the gaps correspond to completely filled and empty LLs, hence the gate voltage values corresponding to the different values of the filling factor $\nu = -10, -6, -2, 2$. Those values are converted into charge carrier density values n in Fig. S2B using :

$$\nu = n\phi_0/B \tag{3}$$

with $\phi_0 = h/e$ the flux quantum. A polynomial of degree 5 is used to fit these points and to interpolate the evolution of the charge carrier density in the range of gate voltage of the gate map. From this fit, charge neutrality at $n = 0$ is achieved at $V^{CNP} = 13.5$ V. We use the field-effect relation $en = C_g(V_g - V^{CNP})$ with the gate capacitance $C_g = \epsilon_0\epsilon_r/d_{STO}$ to obtain the equation linking the back-gate insulator relative dielectric constant ϵ_r to the carrier density n and the gate voltage V_g :

$$\epsilon_r = \frac{d_{STO}}{\epsilon_0}\frac{en}{V_g - V^{CNP}} \tag{4}$$

The red curve in Fig. S2B shows the resulting ϵ_r, which decreases with increasing gate voltage and ranges between 12 500 and 3 500. A similar $\epsilon_r(V_g)$ profile but with slightly weaker values is obtained for sample AC23 ($3\,000 < \epsilon_r < 11\,500$). Finally, using the fit of the filling factor ν, we can rescale the gate map as a function of ν which is shown in Fig. S2C. In particular, note that in the rescaled map the interaction-induced gap is maximal at charge neutrality $\nu = 0$, as expected considering that the exchange interaction is maximal at half-filling of the zeroth Landau level.

V. LANDAU LEVELS OF DIRAC FERMIONS

We show in Fig. S3A a tunneling conductance $\mathrm{d}I_\mathrm{t}/\mathrm{d}V_\mathrm{b}$ spectrum taken on sample STO07 ($SrTiO_3$) at $B = 14\,\mathrm{T}$ (same than Fig. 2B of the main text), where graphene was brought to charge neutrality with a gate voltage $V_\mathrm{g} = 13\,\mathrm{V}$ using the $\mathrm{d}I_\mathrm{t}/\mathrm{d}V_\mathrm{b}$ gate maps from Fig. 2A. Additionally, Fig. S3B displays a spatially-averaged $\mathrm{d}I_\mathrm{t}/\mathrm{d}V_\mathrm{b}$ spectrum on a $100 \times 100\,\mathrm{nm}^2$ area around the same position as Fig. S3A, where we clearly see well-resolved Landau levels in the local density of states (LDOS) up to $N = \pm 6$ as well as both peaks of the LL_0 broken-symmetry state, with a gap of $\Delta E^{\nu=0} \simeq 36\,\mathrm{meV}$. We fit in Fig. S3C the positions E_N of the Landau levels as a function of $(|N|B)^{1/2}$ ($E_0 \approx 0.7\,\mathrm{meV}$ is taken at the middle of the LL_0 peaks). We obtain an excellent agreement with the theoretical dispersion relation for graphene :

$$E_N = E_\mathrm{D} + \mathrm{sign}(N) v_\mathrm{F} \sqrt{2\hbar e |N| B} \tag{5}$$

confirming the massless behavior of charge carriers in graphene. The fit yields a Fermi velocity of $v_\mathrm{F} = (1.403 \pm 0.005) \times 10^6\ \mathrm{m.s}^{-1}$. This value is much greater than the expected theoretical one of $1.0 \times 10^6\ \mathrm{m.s}^{-1}$, which we attribute to the enhancement of electron-electron interactions at charge neutrality [24, 25, 52].

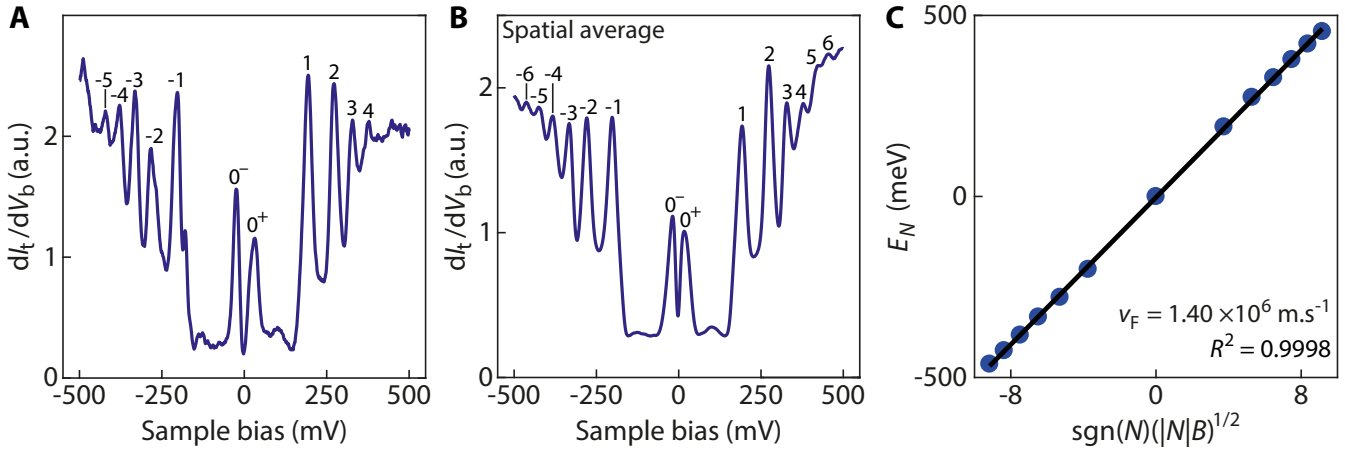

FIG. S3. **Relativistic Landau levels in graphene in sample STO07 on $SrTiO_3$** (**A**) Individual tunneling differential conductance $\mathrm{d}I_\mathrm{t}/\mathrm{d}V_\mathrm{b}$ spectrum at $B = 14\,\mathrm{T}$ and $V_\mathrm{g} = 13\,\mathrm{V}$ showing well-defined Landau level peaks. The zeroth Landau level is split into two peaks $\mathrm{LL}_0{}^{\pm}$. (**B**) Spatially-averaged $\mathrm{d}I_\mathrm{t}/\mathrm{d}V_\mathrm{b}$ spectrum under the same conditions on a $100 \times 100\,\mathrm{nm}^2$ area. (**C**) Fit using Equation (5) of the positions of Landau levels E_N as a function of $(|N|B)^{1/2}$ with N the Landau level index. An excellent agreement is obtained and the fit yields a Fermi velocity $v_\mathrm{F} = (1.403 \pm 0.005) \times 10^6\ \mathrm{m.s}^{-1}$.

VI. TUNNELING CONDUCTANCE GATE MAPS AND INTERACTION-INDUCED GAP IN SAMPLE AC04

We show in Fig. S4 some examples of ΔE^0 estimations at different magnetic fields B for the sample AC04 ($\mathrm{Gr/hBN/SiO_2}$) which were reported in Fig. 2E of the main text. ΔE^0 is computed as the maximum value of the peak-to-peak energy between $\mathrm{LL}_{0\pm}$ extracted from the individual spectra of the gate map.

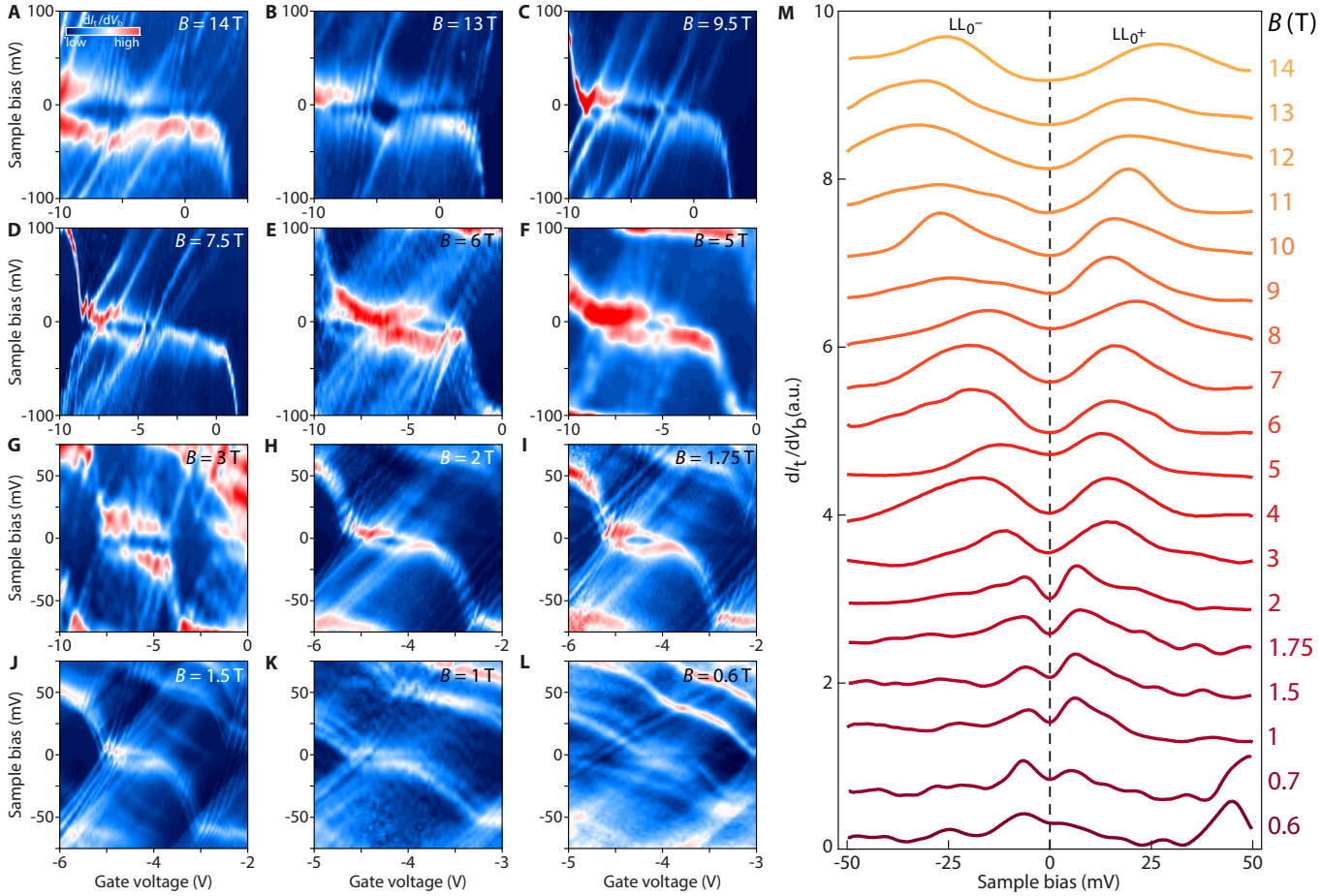

FIG. S4. **Evolution of ΔE^0 with the magnetic field on hBN/SiO$_2$,** in sample AC04. (**A-L**) Tunneling conductance, $\mathrm{d}I_\mathrm{t}/\mathrm{d}V_\mathrm{b}$, gate maps at different magnetic fields. (B,C) were performed at the same position, same for (H-L). (**M**) Some $\mathrm{d}I_\mathrm{t}/\mathrm{d}V_\mathrm{b}$ spectra around (and centered at) zero bias we used to estimate ΔE^0 from $\mathrm{d}I_\mathrm{t}/\mathrm{d}V_\mathrm{b}$ gate maps at different magnetic fields B.

VII. TUNNELING CONDUCTANCE GATE MAPS AND INTERACTION-INDUCED GAP IN SAMPLE STO07

Figure S5 shows the evolution of the tunneling conductance $\mathrm{d}I_\mathrm{t}/\mathrm{d}V_\mathrm{b}$ gate maps for decreasing magnetic fields from $B = 14$ T to $B = 1$ T in sample STO07 ($SrTiO_3$ substrate). For each magnetic field, we perform the same gate sweep from $V_\mathrm{g} = 80$ V to $V_\mathrm{g} = -20$ V in order to keep the hysteresis cycle of the $SrTiO_3$ substrate constant. The full $\mathrm{d}I_\mathrm{t}/\mathrm{d}V_\mathrm{b}$ gate map at $B = 14$ T is shown in panel (A), and the zoom on the yellow rectangle centered on the LL_0 gap is displayed in panel (B). The next panels are zooms on the same area as (B). All those $\mathrm{d}I_\mathrm{t}/\mathrm{d}V_\mathrm{b}$ gate maps were acquired at the same position on graphene, up to the magnetic field drift.

Let us start at $B = 1$ T in the bottom right panel. Many peaks dispersing negatively with the gate voltage are visible, among them we can already distinguish LL_0 and LL_1. With increasing magnetic fields, other resonant peaks eventually merge with each other to form LLs, as described in Ref. [53]. For instance LL_2 is formed at $B = 3$ T while LL_{-1} becomes distinguishable at $B = 5$ T. We also notice at $B = 1$ T that there is no pinning effect of E_F inside LLs, which thus disperse continuously with the gate voltage. LLs start to pin the Fermi level at $B = 3$ T with the formation of a small plateau for LL_0 at $V_\mathrm{g} = 27.5$ V. However note that the splitting of LL_0 in panel (M) is mostly due to the lifting of the orbital degeneracy [54], such that the apparent gap at zero bias (indicated by the green arrow) may be different from the interaction-induced gap we are aiming for. This orbital splitting is maximum at $B = 4$ T and then decreases at higher magnetic fields.

The gap ΔE^0 finally opens at $B = 5$ T, see the yellow arrow in panel (K). Since the density of states of LL_0 grows with B, the Fermi level stays pinned inside LL_0 for a wider range of gate voltage with increasing B, and as a result the

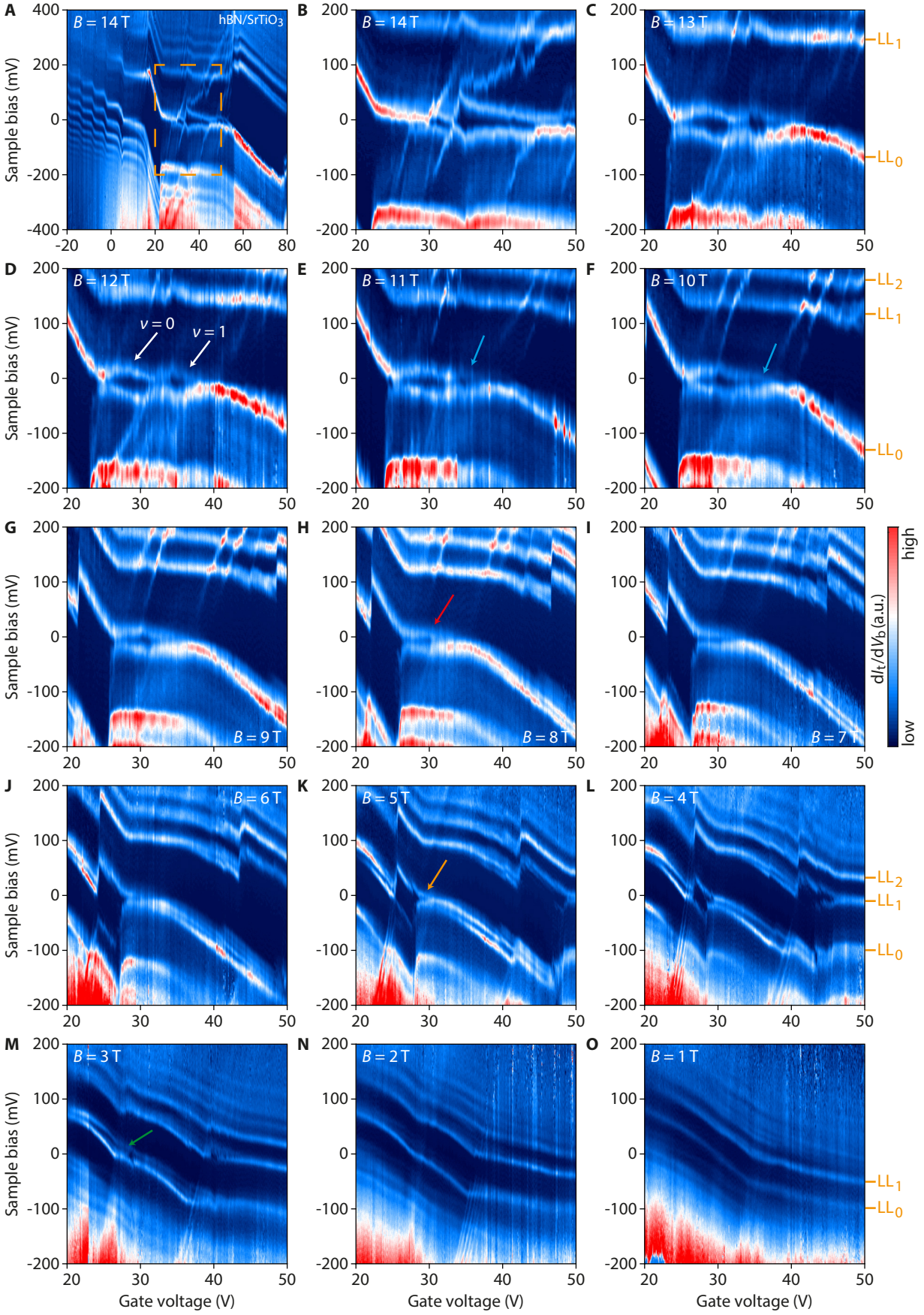

FIG. S5. **LDOS gate maps as a function of the magnetic field B on hBN/$SrTiO_3$,** in sample STO07 and at the same position.

gap develops on a larger LL_0 plateau. At $B = 8$ T the gap features a maximum due to its enhancement by exchange interactions, see the red arrow in panel (H). At $B = 10$ T, a second maximum appears on the right extremity of the LL_0 plateau, see the blue arrow in panel (F), while at $B = 12$ T we clearly distinguish two lobes marked by the white arrows in panel (D). The left lobe corresponds to the opening of the $\nu = 0$ gap whereas the right one is due to the opening of the $\nu = 1$ gap (however the $\nu = -1$ gap is not visible).

VIII. KEKULÉ BOND ORDER IN Gr/hBN/SiO_2 SAMPLES

We detail in this section the asymmetry of the Kekulé bond (KB) order, its bias dependence and stability in time.

A. Asymmetry of the KB pattern

We compute the 2D FFT of the STM image in Fig. S6A with an asymmetric KB pattern and filter it by considering only certain peaks of the FFT, see Fig. S6B. The 2D FFT is mainly comprised of three hexagons, defined by the yellow, red and blue encircled-peaks. We first filter the STM image by considering the yellow peaks only, which yields the usual honeycomb lattice in (C). We now filter with the red peaks only, and obtain the image shown in (D) which features a triangular lattice. When we superimpose the KB lattice drawing, we notice that each bright point of the triangular lattice in (D) falls either on the strong white bonds of the Kekulé lattice or at the center of the hexagons devoid of strong bond : the addition of both images yields the bond-density wave as shown in (E) where we have filtered the STM image by considering this time both yellow and red peaks and mostly recovered the original KB pattern. This also justifies why the hexagon devoid of strong bond in the KB pattern appears brighter than the neighboring hexagons comprised of three strong bonds, similarly visible in Fig. 4A of the main text. Note that the presence of two red peaks with halved amplitude in one direction is responsible of the slight asymmetry that is already visible in Fig. S6E.

We show in Fig. S6F the image obtained after filtering using only the blue peaks. We observe a strongly asymmetric triangular lattice encoding the Kekulé spatial modulation at $\sqrt{3}$ times the graphene lattice parameter. The asymmetry arises from a large asymmetry between the blue peaks in the FFT, where two peaks in one direction are twice as high as the others. This yields dissimilar weights to the bond-density wave, as shown in Fig. S6G where we have filtered considering red and blue peaks, and explains the strong asymmetry we observe in the KB pattern, which is fully recovered in Fig. S6H where we have filtered with the yellow, red and blue peaks. We conjecture this strong asymmetry of the FFT originates from the existence of the K-CDW order whose contribution is visible in Fig. S6F,

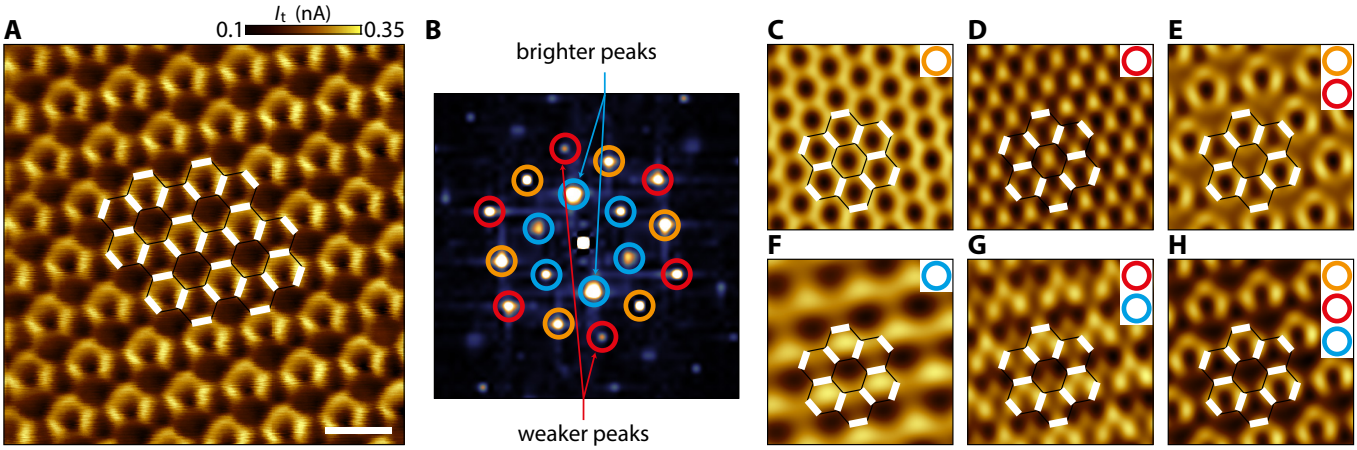

FIG. S6. **FFT decomposition of the asymmetric Kekulé distortion.** (**A**) $3 \times 3\,\mathrm{nm}^2$ image at $B = 14$ T and $V_b = 2$ mV showing an asymmetric KB pattern. (**B**) 2D FFT of the STM image in (A), with peaks marked by circles of different colors : yellow for the honeycomb lattice, red and blue for the bond-density wave. (**C-H**) Filtered images obtained by considering certain peaks of the FFT as indicated in the top right corner of each panel. The Kekulé lattice is drawn in white for reference. The KB order is mostly retrieved by considering only the yellow and red peaks. The asymmetry of the KB pattern is encoded in the blue peaks whose two of them are twice as high as the others due to the K-CDW order. Scale bar : 500 pm.

since in symmetric KB pattern (where this long-range CDW order is not visible) there is no such asymmetry between the blue and red peaks.

B. Bias dependence of the KB order

We show in Fig. S7 constant height STM images where we have changed the sample bias V_b as the scan was in progress. The arrows on the right of each panel show the direction of the slow axis of the scan, and their color corresponds to the actual sample bias which is indicated in the bottom insets. In Fig. S7A we clearly observe the contrast inversion when switching the sample bias from LL_{0^+} to LL_{0^-}, with the continuity of the KB pattern at the interface. In Fig. S7B we clearly see the transition from the usual honeycomb lattice to the KB pattern when switching the sample bias from LL_1 to LL_{0^+}.

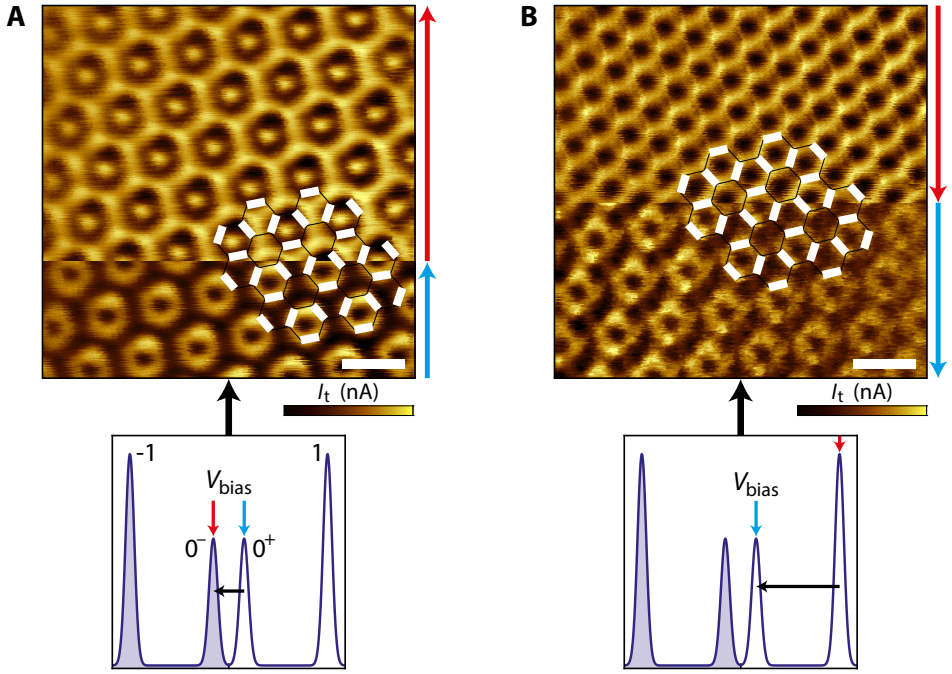

FIG. S7. **Contrast inversion and emergence of the Kekulé bond order.** $3 \times 3\,\mathrm{nm}^2$ current STM images during which we changed the bias voltage as shown in the bottom insets (the current color bars are tuned separately for each half of the images). (**A**) We start (bottom) at $V_b = 32$ mV (LL_{0^+}) and switch (top) to $V_b = -12$ mV (LL_{0^-}) to observe the contrast inversion of the KB lattice. (**B**) We start (top) at $V_b = 200$ mV (LL_1) and switch (bottom) to $V_b = 20$ mV (LL_{0^+}) to observe the emergence of the KB order from the honeycomb lattice. Scale bar for both images : 500 pm.

C. Moving domain walls in the K-CDW order

We show in Fig. S8 three successive images acquired in a row at the same position and at sample bias $V_b = 2$ mV. The blue arrows on the left of each image indicate the direction of the slow axis of the scanning. Figure. 4D of the main text belongs to the same set of image acquisition. The lattice in overlay describes the asymmetric KB pattern, with the white links being the strong bonds of the KB order, whereas the asymmetry that comes from the K-CDW order makes the hexagons with blue weak bonds brighter than the hexagons with red weak bonds. The next image in panel (B) (duration of each image : 53 seconds) starts from the bottom, where we observe the same KB pattern. However a jump occurs at the line indicated by the red arrows, and after that, in the top part of the image, the asymmetry of the KB pattern is reversed : using the lattice in overlay as a guide for the eye, we see that the red hexagons are brighter (due to the three strong white bonds almost merging together), such that the new pattern is the mirror of the previous one. Eventually, the next image in panel (C) displays this new pattern with brighter red hexagons on the whole area, and the next images we realized during several minutes happened to be identical. This indicates that the K-CDW order transited and reversed the asymmetry of the KB phase. Note that the pattern of

the strong white bonds, which defines the KB order, stays unchanged in the three images (in opposition to the KB order transition shown in Fig. 4F and G of the main text).

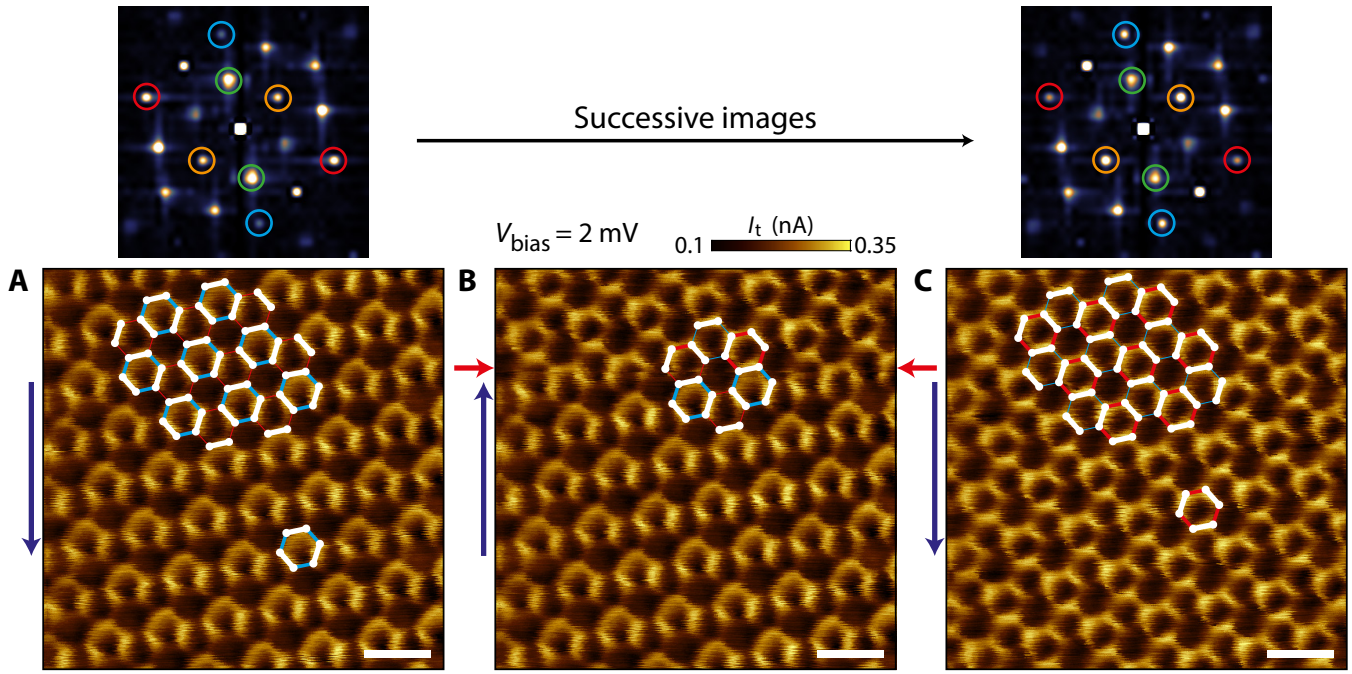

FIG. S8. **Moving wall in the Kekulé pattern.** $3 \times 3\,\mathrm{nm}^2$ current STM images at $B = 14\,\mathrm{T}$, $V_\mathrm{b} = 2\,\mathrm{meV}$ and at the same position. The three images were measured successively in a row (scanning time : 1 min). A jump occurs in (B) at the red arrows and reverses the asymmetry of the Kekulé pattern. The slow axis direction of the scanning is indicated by the blue arrows on the left of each image. Scale bar for the three images : 500 pm.

The asymmetry reversal of the KB order due to the K-CDW transition is well seen in the 2D FFT of both images in Fig. S8A and C, see top insets. For panel (A), the K-CDW appears in the inner hexagon, where the two peaks encircled in green are twice as bright as the other four peaks. On the contrary, for panel (C), this is now the yellow peaks which are brighter than the other four, with the amplitude of the green peaks lowered. The change of the direction of the two brighter peaks induces the change of the asymmetry pattern of the KB order. Interestingly, the outermost hexagon, which corresponds to the bond-density wave, also features a change in the intensity of its peaks : in panel (A) the blue peaks are halved in amplitude while in panel (C) this is the red peaks which are halved. This does not yield any significant change of the KB pattern but this may mean that the bond-density wave and the long-range charge-density wave are entangled.

Therefore, the asymmetry of the KB patterns we observed strongly depends on the time fluctuations of the K-CDW order. Moreover, the fact that we captured the line with the jump in panel (B) could indicate a moving domain wall, and thus the existence of domains with different polarizations of the K-CDW. Note that this only concerns this anomalous K-CDW which coexists with the KB order, the later being unchanged in the three images (the bright bonds pattern remains the same).

Such transitions of the K-CDW happened a few times during our measurements. In Fig. S9A we show a $10 \times 10\,\mathrm{nm}^2$ image of asymmetric KB pattern with the circle-like pattern formed by the merging of the strong bonds inside one hexagon of the KB order unit cell. Imaging the same area a few minutes later in Fig. S9B unveils a domain wall indicated by the red arrows : in the top part, the three strong bonds merge together inside another hexagon of the KB order unit cell with respect to the bottom part (see the white dashed line which intercepts the circles in the top part of the image and, conversely, passes between the circles in the bottom part). As previously, the KB order lattice itself does not change.

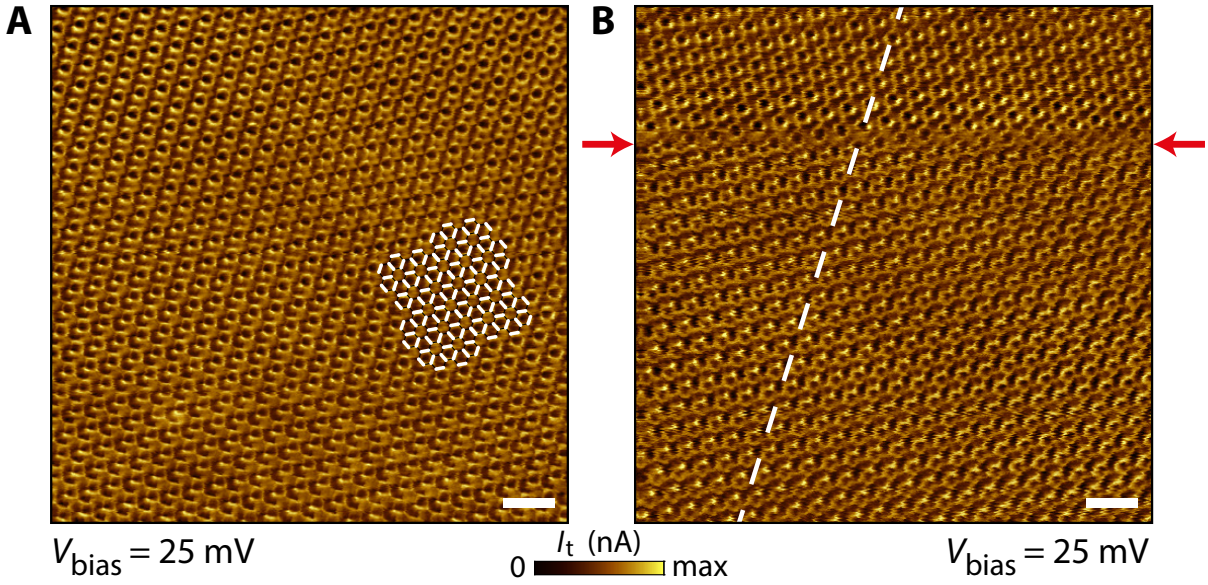

FIG. S9. **Variation of the Kekulé asymmetry.** $10 \times 10\,\mathrm{nm}^2$ current STM images at $B = 14\,\mathrm{T}$ and $V_\mathrm{b} = 25\,\mathrm{meV}$. In (**B**) the asymmetry pattern changes at the domain wall indicated by the red arrows. Scale bar for both images : 1 nm.

IX. INDUCED t_2 ASYMMETRY IN THE CHARGE-DENSITY-WAVE STATE

We start by discussing how a second nearest-neighbour hopping asymmetry gaps the zeroth Landau level (zLL) of graphene. We consider the spinor $\psi = (\psi_{AK}, \psi_{BK}, \psi_{AK'}, \psi_{BK'})$, where $\psi_{\sigma\tau}$ is a zLL single-particle wavefunction in sublattice σ and valley τ. In this basis, both the sublattice imbalance $\Delta n = n_A - n_B$ and the second nearest-neighbor hopping asymmetry $\Delta t_2 = t_{2,A} - t_{2,B}$ (see Fig. S10) enter the low energy Hamiltonian close to the Dirac point with the matrix $\tau_0 \otimes \sigma_z$ in valley (τ) and sublattice space (σ). This matrix structure implies that both perturbations gap out the K and K' points of graphene, with a gap given by [30] :

$$E_\mathrm{g} = \Delta n + \frac{3}{2}\Delta t_2, \tag{6}$$

which is of equal sign for both valleys. We can visualize the effect of Δt_2 and Δn on the zeroth Landau level by diagonalizing the graphene Hamiltonian in the presence of a magnetic field. The spectrum with $\Delta t_2 \neq 0$ and $\Delta n \neq 0$ are shown in Fig. S10 A and B respectively, obtained with the KWANT package [55]. We can confirm numerically that the gap is given by Eq. (6) and that when $\Delta n = -\frac{3}{2}\Delta t_2$ the gap closes, confirming that both perturbations enter the Hamiltonian with the same matrix structure.

The above argument suggests that interactions that induce a finite Δn will generically induce a finite $\Delta t_2 \neq 0$, as they both enter with the same matrix structure. To exemplify this generic behavior we use the Hamiltonian of graphene in the presence of nearest-neighbor interactions V_1 :

$$H = t \sum_{\langle ij \rangle} \left(c_i^\dagger c_j + \mathrm{h.c.} \right) + V_1 \sum_{\langle ij \rangle} n_i n_j, \tag{7}$$

where the sums are taken over nearest neighbors of the honeycomb lattice. Note in particular that the second-nearest neighbor hopping is explicitly zero in the Hamiltonian. In the limit of infinitely large interaction, the ground state of H at half-filling is a charge-density wave with one fully occupied and one fully empty sublattice, a state characterized by $\Delta n = 1$. The bond asymmetry Δt_2 is expected to be exactly zero in this limit, since all sites on one sublattice are completely full and thus no states are available to hop to. Similarly, all sites on the other sublattice are completely empty such that no states are available to hop from. At sufficiently large (but finite) V_1/t the ground-state is a charge-density wave with partial sublattice imbalance , as we numerically show in Fig. S11. In Fig. S11A, we show the expectation value of Δn in the ground-state of H for different V_1 obtained by using the infinite density matrix renormalization group (iDMRG), implemented using the TENPY package [56], as explained in Ref. [28]. For small interactions Δn is close to zero, and grows continuously to one as V_1 is increased, signaling a second order-phase

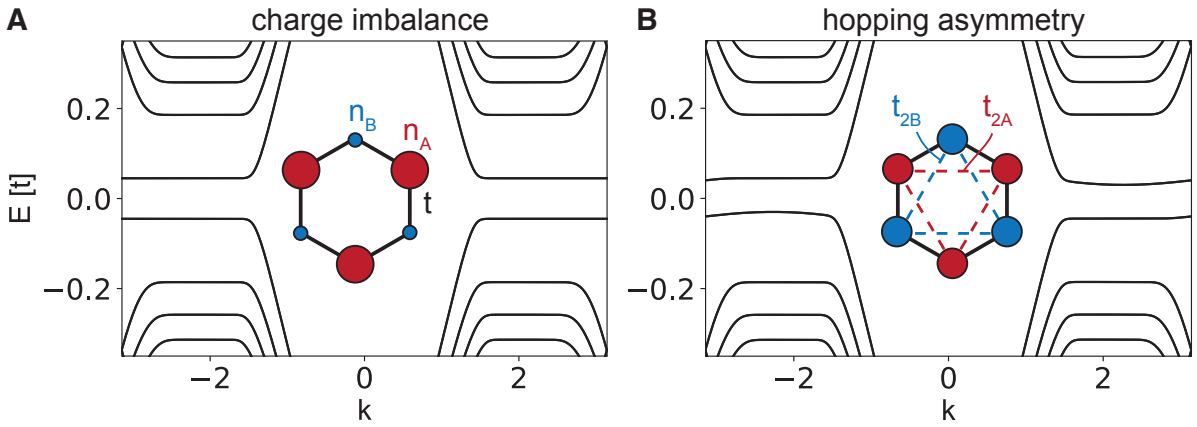

FIG. S10. **Effect of sublattice charge imbalance and a t_2 asymmetry on the zeroth Landau level.** (**A**) shows that the effect of a finite charge imbalance $\Delta n = n_A - n_B$ is to gap the zeroth Landau Level of graphene. Panel (**B**) shows that a hoping asymmetry $\Delta t_2 = t_{2,A} - t_{2,B}$ also opens up a gap, that depends on momentum k as we move away from the K and K' points. The parameters are chosen so that E_g is the same on both plots at the K and K' points, according to (6). Simulations were performed using the KWANT software[55] for a 41×41 hexagonal lattice with $\phi = 0.003$ flux per plaquette, in units of the flux quantum. Energies are measured in units of the nearest-neighbor hopping t. For **A** $\Delta t_2 = 0$ and $\Delta n = 0.045$, while for **B** $\Delta t_2 = 0.015$ and $\Delta n = 0$.

transition (see e.g. Ref. [28] for a discussion). As shown in Fig. S11B, we observe a concomitant bond asymmetry Δt_2 that develops at intermediate values of V_1, as expected based on our previous symmetry discussion. As V_1 increases, Δt_2 increases until reaching a maximum, and then decreases as V_1 becomes larger. It is possible to check numerically that setting $t = 0$ in (7), i.e. in the limit $V_1/t \to \infty$, leads to $\Delta t_2 = 0$ and $\Delta n = 1$, as discussed above.

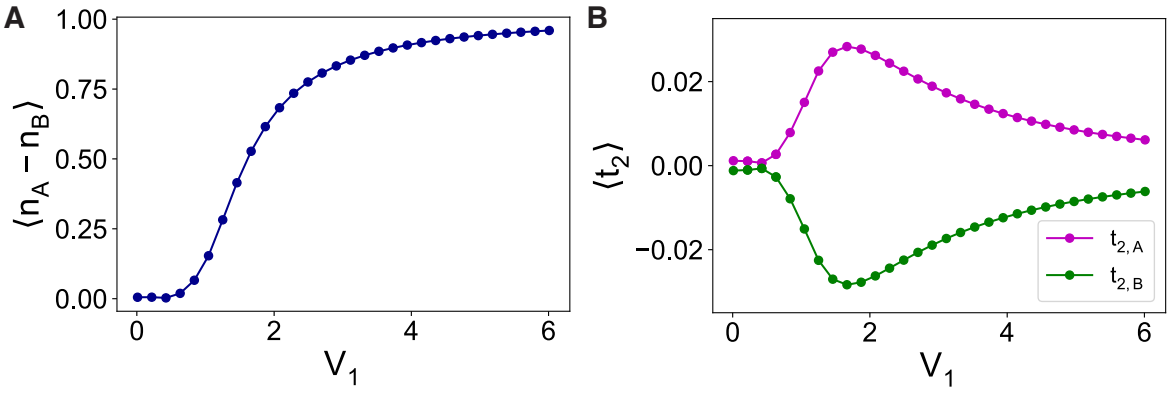

FIG. S11. **Induced Δt_2 asymmetry by interactions.** Panel (**A**) shows that a sublattice charge imbalance develops as V_1 increases. Panel (**B**) shows how a simultaneous asymmetric bond expectation $\Delta t_2 \neq 0$, peaking at intermediate values of V_1. The simulations are carried out using a cylinder circumference of $L_y = 6$ sites and bond-dimension $\chi = 1000$ with the TENPY package [56].

The above results support that a charge-density-wave order with a partial sublattice imbalance, i.e. $0 < \Delta n < 1$, is generically accompanied by a second-nearest-neighbor bond asymmetry, $\Delta t_2 \neq 0$, as argued in the main text.

In the zLL of graphene the wave-functions at each valley live in different sublattices and thus a full valley polarization implies a full sublattice polarization $\Delta n = 1$, in which case $\Delta t_2 = 0$. When the the sublattice polarization is not maximal then a finite Δn and Δt_2 are expected, consistent with what is observed in experiment (see Fig. 5 in the main text). As mentioned in the main text, this effect can originate from Landau level mixing since the sublattice index is not locked to valley index beyond the zLL [31–33].

X. CHARGE-DENSITY WAVE IN Gr/hBN/$SrTiO_3$ SAMPLES

A. Influence of the Moiré superlattice

The sample AC23 displays a weak Moiré superlattice (weak in the sense that is not always visible in our images). This arises the question of whether the CDW phase we observed was induced by the Moiré pattern, which could also break the sublattice symmetry, or not. In such case, we should expect the CDW pattern to rely on that of the Moiré, with the sublattice polarization depending on the position inside the Moiré superlattice (due to the periodic potential it induces in graphene). Figure S12B displays a CDW phase observed at $B = 7\,\mathrm{T}$. The Moiré pattern is barely visible but appears as bright spots, such as the ones indicated by dashed white circles. However the CDW pattern itself is seen not to fluctuate in presence of this Moiré lattice, which as a result rules out the Moiré origin of our CDW phase.

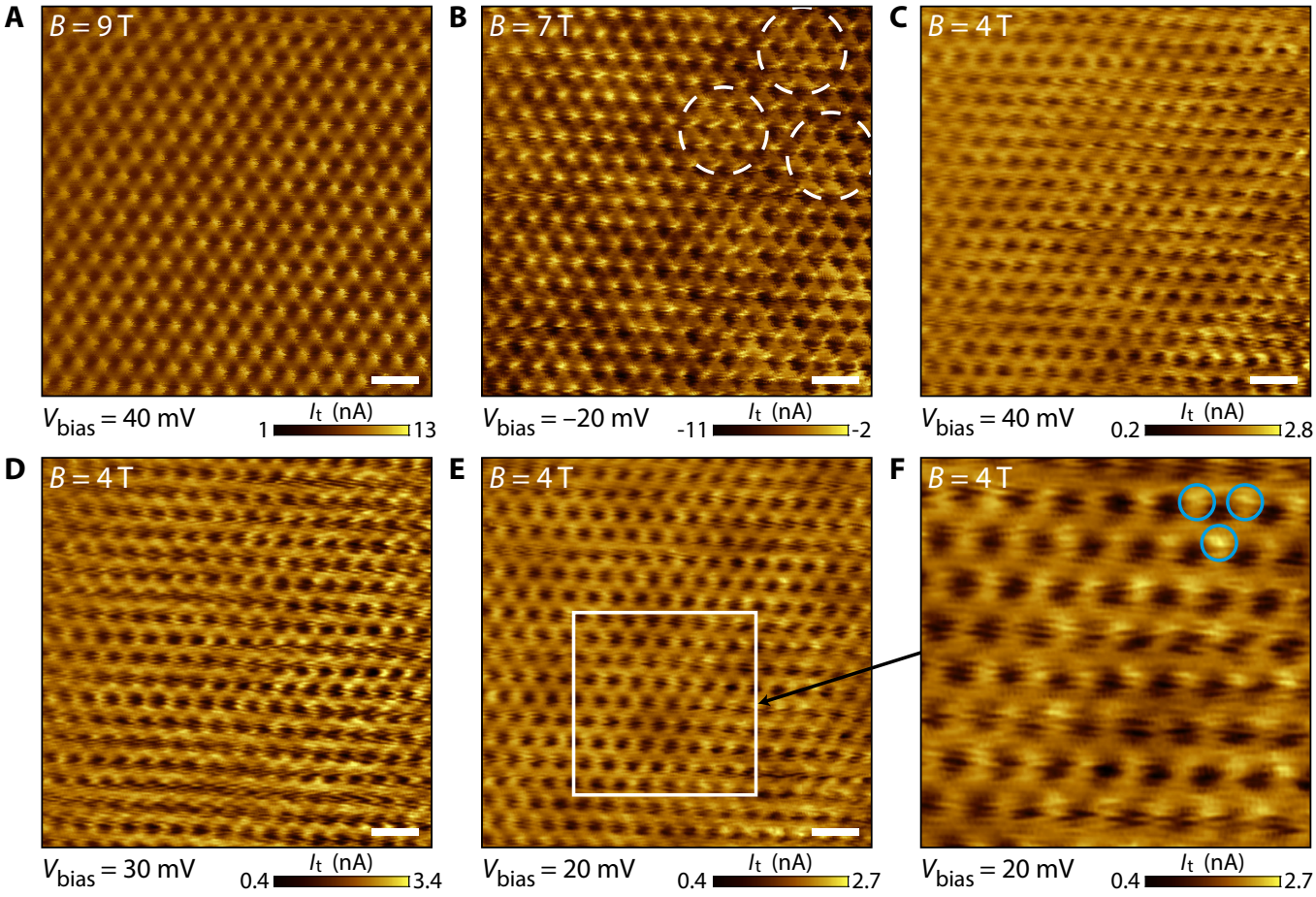

FIG. S12. **Disappearance of the charge density wave at low magnetic field in sample AC23.** (**A**) CDW at $B = 9\,\mathrm{T}$. (**B**) CDW at $B = 7$ T. The Moiré superlattice of sample AC23 is visible but does not perturb the CDW pattern. (**C,D**) Honeycomb lattice with no CDW at $B = 4$ T. (**E**) Honeycomb lattice at $B = 4$ T with residual traces of CDW, see the zoom in (**F**) of the white rectangle. Scale bar for all figures : 500 pm.

We also performed STM measurements in the similar sample AC24 on $SrTiO_3$. Contrary to sample AC23, we never notice any Moiré lattice in this second sample. In the same conditions, at charge neutrality, we observed signatures of a CDW phase, shown in Fig. S13B, which confirms our conclusion that the CDW we observe in our hBN/$SrTiO_3$ samples is indeed an intrinsic consequence of many-body interactions at charge neutrality and not due to extrinsic substrate-induced sublattice symmetry breaking.

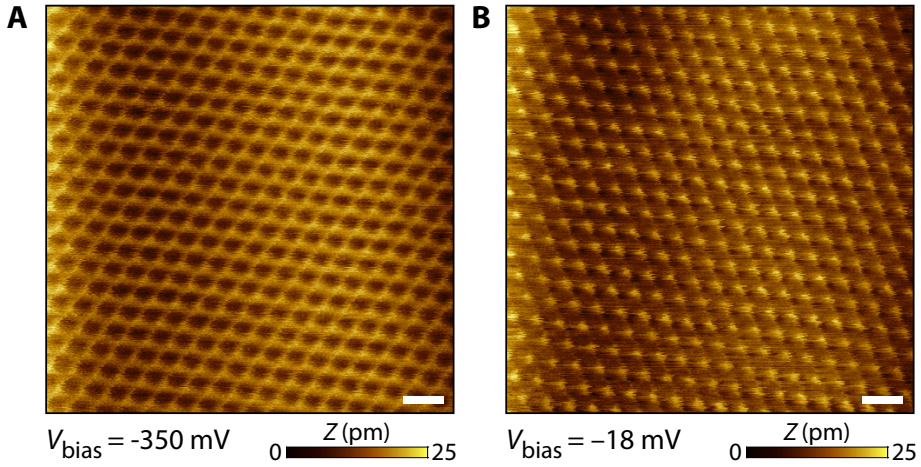

FIG. S13. **Charge-density wave order in sample AC24.** (**A**) Honeycomb lattice at $B = 14\,\mathrm{T}$ and $V_\mathrm{b} = -350\,\mathrm{mV}$ observed in constant-current mode in charge-neutral graphene. (**B**) CDW under the same conditions but at $V_\mathrm{b} = -18\,\mathrm{mV}$. Scale bar for both figures : 500 pm.

B. Disappearance at low magnetic field

Figures S12A and B show that the CDW persists at $B = 9\,\mathrm{T}$ and $B = 7\,\mathrm{T}$. However, Figs. S12C to E at $B = 4\,\mathrm{T}$ does not display the CDW anymore but just the usual sublattice-unpolarized honeycomb lattice.

Finally, it is theoretically expected [14] that graphene undergoes a first-order phase transition from the CDW to the F phase. Such a transition should induce the formation of domains in graphene with the coexistence of both phases around the magnetic field at which the transition occurs. When taking a closer look to Fig. S12E taken at $B = 4\,\mathrm{T}$, see its zoom in Fig. S12F, one can discern that some bright dots appear in some parts of the image (see the blue circles). This residual asymmetry of the honeycomb lattice is reminiscent of a charge-density wave. It is possible that it may constitute a signature of such domains around the transition between the CDW and F phases.